# HYDROGEN PRODUCTION USING A HIGH-EFFICIENCY ALKALINE WATER ELECTROLYZER

**ANA LOURENÇO SILVA DOS SANTOS**

THESIS TO OBTAIN THE MASTER'S DEGREE IN

**CHEMICAL ENGINEERING**

**SUPERVISORS:** Dr. Diogo dos Santos

Dr. Jorge Antunes

**EXAMINATION COMMITTEE**

| | |
|---|---|
| **CHAIRPERSON:** | Dr. Mário Berberan e Santos |
| **SUPERVISOR:** | Dr. Diogo dos Santos |
| **MEMBERS OF THE COMMITTEE:** | Dra. Carmen Rangel |
| | Dra. Maria João Cebola |

**FEBRUARY 2020**

## ACKNOWLEDGMENTS

Firstly, I have to sincerely acknowledge Dr. Diogo dos Santos for trusting me with this thesis and guiding me through this last challenge before I graduate with my master's degree. His willingness to help and follow my work, almost daily, made my job easier every day. I could not ask for a better advisor. Additionally, I would like to thank to every member of the group, who were always available to help me in any matter.

Likewise, I have to demonstrate my sincere gratitude to Eng. Jorge Antunes, CEO of TecnoVeritas, for allowing me to be part of his incredible company and to teach me a lot during this journey. It is an inspiration to hear him speak with such delight about this project. It was a pleasure to have him as a mentor.

Also, I would like to mention Miguel Costeira, from TecnoVeritas, who was like a third supervisor of this thesis. He followed all my work and always demonstrated concern in providing me all the necessary information so that I could present a complete and remarkable work.

To João, my biggest support during these months. I would like to thank him for dealing with all my highs and lows and for constantly hearing about hydrogen and electrolyzers, without often understanding a single word that I was saying.

To my dearest friends, who need no introduction. From college mates, they became life companions. They made the whole college experience memorable.

Above all, I must thank my family. To my father for working so hard so that I could pursue all of my goals and dreams. To my sister, for being a role model, both personally and professionally. I wish to become a woman like her, someday. And to my mother, the woman of my life and the source of all my strength. For believing in me more than I do, sometimes.

## ABSTRACT

Hydrogen is being reported as the key energy carrier to developing a clean and sustainable energy system. Water electrolysis is currently the cleanest method to produce hydrogen. Among the commercially available water electrolysis systems, alkaline water electrolysis (AWE) is the most well-established technology. But for a hydrogen economy to thrive there is still the need to improve AWE efficiency, without compromise the production cost.

The present dissertation is part of the Green$H_2$ice project developed by TecnoVeritas, with the main objective of developing a high-efficiency alkaline water electrolyzer. In this work, the complete electrolyzer system is described. In addition, since the electrodes' catalytic behavior has a great weight in the electrolyte efficiency, the materials chosen for the electrodes were studied to validate their behavior towards the hydrogen evolution reaction (HER) and oxygen evolution reaction (OER). The individual performance of nickel foam (NF) and 316L stainless steel foam (SSF) was studied in a 30 wt.% NaOH electrolyte, towards the HER and OER, respectively, using cyclic voltammetry, linear sweep voltammetry and chronopotentiometry. Furthermore, the performance of the electrodes was also evaluated towards the overall water splitting, in a system with the NF as cathode and the SS foam as anode.

Using the results obtained from the electrochemical studies of the foams, the behavior of the electrolyzer was simulated using MATLAB/Simulink. The theoretical polarization curve was obtained, as well as an estimation of the hydrogen production.

**Keywords:** alkaline water electrolysis, high-efficiency electrolyzer, hydrogen evolution reaction, nickel foam, oxygen evolution reaction, stainless steel foam

## RESUMO

O hidrogénio é visto como o componente-chave para o desenvolvimento de uma rede de energia sustentável. Atualmente, a eletrólise da água é o método mais limpo para produzir hidrogénio. Entre os vários sistemas de eletrólise da água disponíveis comercialmente, a eletrólise alcalina da água é a tecnologia mais avançada do mercado: No entanto é ainda necessário melhorar a sua eficiência, sem comprometer o custo de produção do hidrogénio.

A presente dissertação está incluída no projeto Green$H_2$ice desenvolvido pela TecnoVeritas, com o principal objetivo de desenvolver um eletrolisador alcalino de alta eficiência. Neste trabalho, o eletrolisador é apresentado. Além disso, como o comportamento catalítico dos elétrodos tem um grande peso na eficiência da eletrólise, os materiais escolhidos como elétrodos foram estudados para validar o seu desempenho quanto à reação de evolução do hidrogénio (HER) e de evolução do oxigénio (OER). O desempenho individual de espumas de níquel (Ni) e de aço inoxidável 316L (aço inox) foi analisada num eletrólito com 30 % (em peso) de NaOH, em relação à HER e OER, respetivamente, usando voltametria cíclica, voltametria de varrimento linear e cronopotenciometria. Foi ainda avaliado o desempenho dos elétrodos em relação à eletrólise da água num sistema com a espuma de Ni como cátodo e de aço inox como ânodo.

Utilizando os resultados obtidos no estudo das espumas, simulou-se o comportamento do eletrolisador recorrendo ao MATLAB/Simulink. Obteve-se a curve de polarização teórica, bem como, uma estimativa da produção de hidrogénio.



**Palavras-chave:** eletrolise alcalina da água, eletrolisador de alta eficiência, reação de evolução do hidrogénio, reação de evolução do oxigénio, espuma de níquel, espuma de aço

## CONTENTS

## LIST OF FIGURES

## LIST OF TABLES

## ABBREVIATIONS

| | |
|---|---|
| $\Delta G_{cell}$ | Gibbs free energy change of the overall cell reaction |
| $\Delta H_{cell}$ | Enthalpy change of the overall cell reaction |
| $\Delta S_{cell}$ | Entropy change of the overall cell reaction |
| AWE | Alkaline water electrolysis |
| $a$ | Activity |
| $b$ | Tafel slope |
| $C_{dl}$ | Double-layer capacitance |
| CC | Carbon cloth |
| CV | Cyclic voltammetry |
| CP | Chronopotentiometry |
| DC | Direct current |
| $E_a$ | Activation energy |
| $E^e_{anode}$ | Equilibrium potential of the anode |
| $E^e_{cathode}$ | Equilibrium potential of the cathode |
| $E_{cell}$ | Cell potential |
| $E^e_{cell}$ | Equilibrium cell voltage |
| $E_{Tn}$ | Thermoneutral voltage |
| ECSA | Electrochemical surface area |
| $F$ | Faraday constant |
| GHG | Greenhouse gases |
| $H_{ads}$ | Adsorbed hydrogen |
| HER | Hydrogen evolution reaction |
| HHV | Higher heating value |
| $iR_{cell}$ | Potential drop |
| $j$ | Current density |

| | |
|---|---|
| $j_{dl}$ | Average capacitive current |
| $j_0$ | Exchange current density |
| LOHCs | Liquid organic hydrogen carriers |
| LSV | Linear sweep voltammetry |
| Mtoe | Million tonnes of oil equivalent |
| $n$ | Number of mols |
| NF | Nickel foam |
| OCP | Open circuit potential |
| OER | Oxygen evolution reaction |
| PEM | Proton exchange membrane / Polymer electrolyte membrane |
| $R$ | Gas constant |
| RT | Room temperature |
| SOEC | Solid oxide electrolysis cell |
| SS | Stainless steel |
| SSM | Stainless steel mesh |
| $T$ | Temperature |
| $\alpha$ | Transfer coefficient |
| $\eta$ | Overpotential |

# 1 INTRODUCTION

## 1.1 BACKGROUND

Due to population increase, growing energy demand poses a severe threat to the global economy, environment, and consequent climate change. Every economic sector is entirely reliant on access to energy. In 2018, the overall consumption of energy was 13.865 Mtoe (million tonnes of oil equivalent) [1] and was expected to grow by nearly 50 % between 2018 and 2050 [2].

Currently, 81 % of the total primary energy supply and 66 % of electricity generation are based on fossil fuels, with oil being the most used resource [3]. As these sources are non-renewable and the extraction and consumption of energy are at such a large scale, their reserves are expected to last for a limited time: 50 years of both oil and natural gas remaining and 150 years of coal production [1]. If this scenario materializes, the world economy can come to a halt. Besides, it is imperative to be concerned about the pollution resulting from fossil fuels' consumption. The massive emission of greenhouse gases (GHG) causes a substantial negative impact not only on the health and quality of life of the population but also on the environment. Atmospheric levels of $CO_2$ are at the highest levels ever recorded; in 2018, the concentration of carbon dioxide reached 407.8 parts per million [4]. The combined land and ocean temperatures have increased at an average rate of 0.18 ºC per decade since 1981 [5].

In 2016, the Paris Agreement was signed in the United Nations Framework Convention on Climate Change, intending to keep the increase in global average temperature to well below 2 ºC, preferable at 1.5 ºC. It was agreed to reduce the carbon emissions, starting at the end of 2020, and reach carbon-neutrality by 2050 [6]. The European Union was the first economy to demand more ambitious targets, with the current goal of reducing $CO_2$ emissions by 40 % by 2030 [7].

Hydrogen is being reported as a critical component to developing a clean and sustainable energy system, that fulfills decarbonizing the atmosphere [7–9]. Hydrogen can be used as a feedstock, a fuel, an energy carrier and storage, and many possible applications across industry, transport, power, and building sectors – Figure 1. It is the most abundant element in the universe; however, it is not readily available in elemental form. It is considered superior compared with other fuels because it can be consumed in various ways other than flame combustion, like direct steam production, chemical conversion, and using fuel cells. It also can store a significant amount of energy in a relatively small amount of hydrogen because of its high energetic yield of 122 kJ $kg^{-1}$, more than twice that of the most conventional fuels. Furthermore, it is 2.5 times more efficient than gasoline due to its specific weight of 0.0899 kg $Nm^{-3}$ [8].

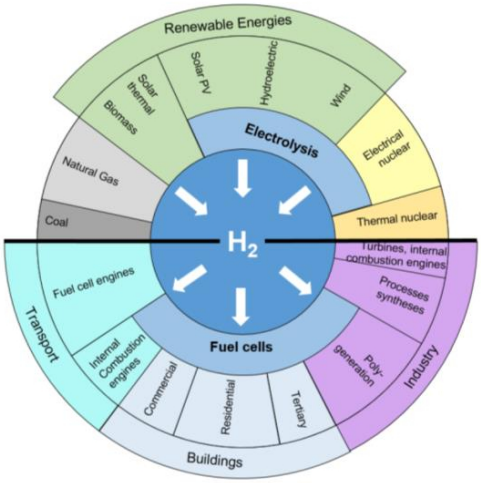


**Figure 1 - Diagram of the hydrogen production and use in a hydrogen economy. Adapted from [10].**

Hydrogen can be classified as grey, blue or green hydrogen, depending on its feedstock and carbon emissions – Figure 2. Naturally, green hydrogen is preferable since it comes from renewable energy and meets the no carbon emission goal [11].

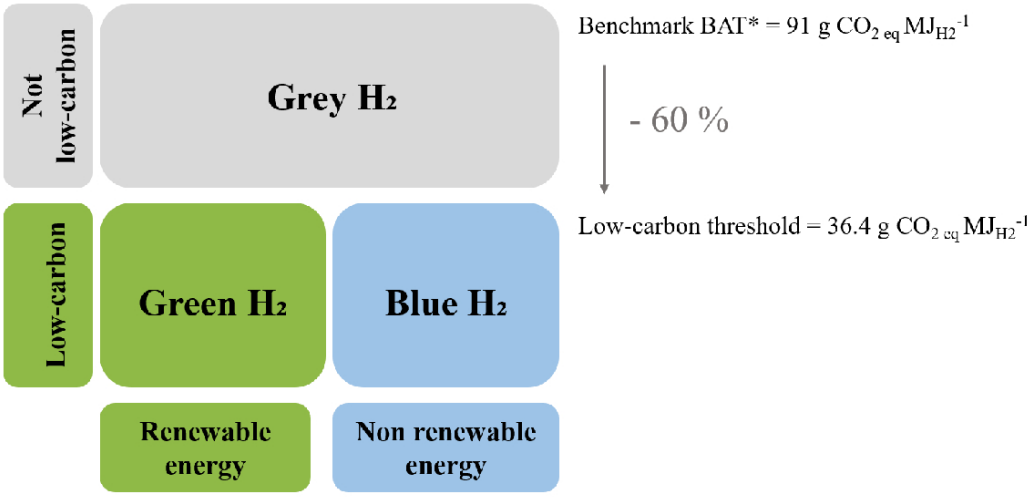


**Figure 2 – Grey, blue, and green hydrogen. *BAT = Best Available Technology – Natural gas steam methane reforming. Adapted from [11].**

Yet, today, hydrogen represents a modest fraction of the global energy mix. Around 70 million tonnes of hydrogen are consumed per year [12], mostly produced from fossil fuels, in specific from steam reforming of natural gas (48 %) followed by oil and coal gasification (30 % and 18 %, respectively). Only 4 % of the global hydrogen supply results from clean sources [9]. Production of hydrogen following a fossil fuel approach benefits from the technologies' maturity and high development, being considered the most cost-effective method. However, from an environmental point of view, these methods are not sustainable for much longer, and there is the need to replace them with cleaner alternatives [13].

Currently, water electrolysis is the leading process among the technologies that use renewable energies to produce hydrogen. The first commercial method of obtaining hydrogen ever developed, and, facing

the new optical of environment care and GHG emissions mitigation, is taking back relevance against fossil fuel-based technologies [14]. From 2010 to 2018, electrolyzer capacity grew about 100 MW [15], reaching the current capacity of 8 GW [12], proving that water electrolysis is increasingly seen as a promising alternative to fossil fuels.

Hydrogen produced from water electrolysis benefits from the zero pollutant emissions generated and the abundance of water resources. In addition, the hydrogen obtained has a high level of purity of 99.99 % [8].

A variety of water electrolysis systems have been proposed over the years. Among the commercially available water electrolysis systems, alkaline water electrolysis (AWE) comprises by far the highest production rate and the lowest production cost, making the this technology the current standard for large-scale water electrolysis systems [13].

Nevertheless, for a hydrogen economy based on water electrolysis to thrive, the scientific community still needs to deepen the knowledge about the subject. Hydrogen produced from this technology must compete with the relatively low prices of the hydrogen produced from fossil fuels. So, there is an urgency in exploring new ways to reduce production costs and improve the efficiency of water electrolysis technologies and new solutions for storage and transportation [16]. The total hydrogen produced only represents around 2 % of the total primary energy demand [8], which means that there is still a long way to go until hydrogen becomes the principal fraction of the global energy system.

## 1.2 GOALS

The present dissertation is part of a project called Green$H_2$ice, initiated in March 2018 by TecnoVeritas in collaboration with OZ Energia S.A and the National Energy and Geology Laboratory (LNEG).

The project's overall proposal is to research and develop an integrated high-efficiency green hydrogen production station for vehicle supply, mainly through the design of a new electrolyzer and a new process for converting internal combustion engines to run with hydrogen. The project includes the following tasks:

- Study, design, and construction of a hydrogen production system and its storage.
- Conception, design, and construction of a high-efficient AWE prototype, addressing efforts to reduce the causes of the most common lack of efficiency of common electrolyzers.
- Pioneering integration and exploratory combination for the production, storage, and dispensing of hydrogen in a safe, environmentally friendly, and economically viable way.
- Conversion of an internal combustion car engine to hydrogen, allowing the use of low-purity hydrogen at low cost, with the consequent reduction of atmospheric effluents.
- Monito and manage the hydrogen production, storage, and distribution process using technologies from industry 4.0.

The first objective of this work was to investigate the parameters related to the AWE's efficiency and incorporate the knowledge gained to develop a high-efficient AW electrolyzer. Since the electrodes' catalytic behavior has a great weight in the electrolyte efficiency, the materials chosen for the electrodes were studied to validate their behavior towards the HER and OER. The influence of temperature in the electrolysis was also studied.

In addition, part of this work was to do a HAZOP analysis of the complete electrolysis system projected, intending to identify and evaluate potential hazards and operability problems in the system before the operation starts.

Lastly, it was expected to observe the developed electrolyzer's performance, analyzing its polarization curve and hydrogen production, varying some characteristics, such as the electrolyte concentration, system pressure, and electrolyzer configuration (in series or parallel), and model their theoretical behavior in MATLAB/Simulink.

# 2 LITERATURE REVIEW

## 2.1 WATER ELECTROLYSIS TECHNOLOGIES

Water electrolysis is not a recent invention and dates back to the 1800s, when William Nicholson and Anthony Carlisle used a voltaic pile for the first time. Over the years, scientists have shown a grown interest in this method, which allowed the development of several technologies.

A raw water electrolysis unit consists of two electrodes immersed in an electrolyte connected through an external power supply. It can have a diaphragm separating both electrodes or not; it depends on the technology.

A direct current (DC) is applied to maintain the electricity balance, and electrons flow from the negative terminal of the DC source to the cathode. The electrons are consumed by hydrogen ions existing in the water, and atoms of hydrogen are formed. The hydroxide ions resulting from the reaction in the cathode move towards the anode surface, where they lose electrons that return to the positive terminal of the DC source, and oxygen is formed. The overall reaction of water electrolysis is Equation (1) [17]:

$$2H_2O\ (l) + energy \rightarrow 2H_2(g) + O_2(g) \quad (1)$$

Pure water is an inferior conductor of electricity, so an acidic or alkaline medium is used as an electrolyte to improve conductivity. Because of that, there is more than one type of electrolyzer, and the half-reactions differ. Nowadays, AWE, polymer electrolyte membrane (PEM) electrolysis, and solid oxide electrolysis cells (SOECs) are the three main types of water electrolysis technologies available. A scheme of these different technologies is presented in Figure 3 [18].

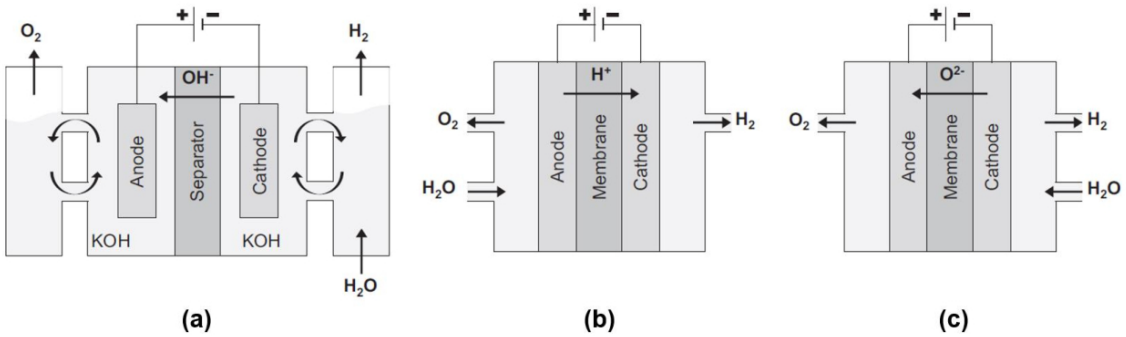


**Figure 3 - Schematic representation of (a) an AWE cell, (b) a PEM electrolysis cell, and (c) a SOEC. Adapted from [19].**

AWE is the oldest and most well-established technology. The cell consists of an anode and a cathode immersed in an alkaline solution, separated by a diaphragm. The hydrogen evolution reaction (HER) at the cathode and the oxygen evolution reaction (OER) at the anode are represented by Equations (2) and (3), respectively.

$$HER: 2H_2O + 2e^- \rightarrow H_2 + 2OH^- \quad (2)$$

$$OER: 4OH^- \rightarrow O_2 + 2H_2O + 4e^- \quad (3)$$

PEM electrolysis is a less mature technology than AWE. PEM electrolysis cells are similar to AWE cells, but they have a solid polymeric membrane with an acidic nature instead of a liquid electrolyte. The membrane, along with the electrodes, form what is called the membrane electrode assembly (MEA). The two characteristic half-reactions are Equation (4) and (5).

$$HER: 2H^+ + 2e^- \rightarrow H_2 \quad (4)$$

$$OER: 2H_2O \rightarrow O_2 + 4H^+ + 4e^- \quad (5)$$

SOEC is the least advanced electrolysis technology, and it is not yet available for commercialization. What distinguishes this technology from the other two is that it is performed at much higher temperatures, as shown in Table 1, where the three processes' main features are compared. SOEC perform the electrolysis of water vapor at high temperatures, resulting in higher efficiencies than the other technologies. The reactions occurring at the cathode and the anode are the following (Eq. 6 e 7 respectively) [13,18,19]:

$$HER: H_2O + 2e^- \rightarrow H_2 + O^{2-} \quad (6)$$

$$OER: 2O^{2-} \rightarrow O_2 + 4e^- \quad (7)$$

The main specifications of the three electrolysis technologies presented are reunited in Table 1.

**Table 1 - Main specifications of the different electrolysis technologies. Adapted from [13,19].**

| Specifications | AWE | PEM | SOEC |
|---|---|---|---|
| Operating temperature / ºC | 60 – 80 | 50 – 80 | 650 – 1000 |
| Operating pressure / MPa | < 3 | < 3 | < 3 |
| Current density / A $cm^{-2}$ | 0.2 – 0.4 | 0.6 – 2 | 0.3 – 2 |
| Cell voltage / V | 1.8 – 2.4 | 1.8 – 2.2 | 0.7 – 1.5 |
| Voltage efficiency / $\%_{HHV}$ | 62-82 | 67 – 82 | 81 – 86 |
| Production rate / $m^3_{H2}$ $h^{-1}$ | < 760 | < 40 | < 40 |
| Specific system energy consumption / kWh $Nm^{-3}$ | 4.3 – 4.8 | 4.4 – 5 | 2.5 – 3.5 |
| Hydrogen purity / % | 99.7-99.9 | 99.999 | 99.9 |
| Cell area / $m^2$ | 3 – 3.6 | < 0.13 | < 0.06 |
| Minimum partial load / % | 10 – 40 | 0 – 10 | - |
| Stack lifetime / kh | 55 – 120 | 60 – 100 | 8 - 20 |
| System lifetime / years | 20 – 30 | 10 – 20 | - |
| System response | seconds | milliseconds | seconds |
| Cold-start time / min | < 60 | < 15 | < 60 |
| Capital cost / € $kW^{-1}$ | 800 – 1500 | 1400 – 2320 | > 2000 |

The three technologies are at different stages of commercialization. AWE and PEM electrolysis are the principal ones used to produce hydrogen from water splitting and already reached commercialization, while SOECs are still in the development stage [55]. For this reason, it will not be the focus of this study.

Being around the longest, alkaline water electrolyzers are sold in more significant numbers despite some superior characteristics offered by PEM. As can be seen in Table 2, PEM electrolyzers provide hydrogen with higher purity. They can reach higher current densities than AWE, without compromising the efficiency [19], due to the tightly-packed structure of the membrane electrode assembly (MEA) and because that the thinner membrane provides higher proton conductivity [18,20]. Also, they have a greater operating range [13].

Despite the advantages, when compared to AWE technologies, PEM technologies have higher costs associated and have shorter stack and system lifetime [17,20]. The polymeric electrolyte membrane is made from an expensive material and have a short durability, which implies a constant replacement. The PEM's short durability is mostly attributed to membrane contamination or chemical self-degradation and deterioration of the anode materials. While in AWE, non-noble metals, such as Ni, are suitable electrocatalysts for HER and OER, in PEM electrolysis, the electrolyte's acidic character implies the use of precious metals as electrocatalysts for the reactions to happen, which increases the investment [21].

These two technologies have always been compared over the years. Researchers from Germany conducted an experience to compare an AW electrolyzer with Ni-based catalysts and thinner separators and a PEM electrolyzer with Ir and Pt-based catalysts and a Nafion membrane. They concluded that an AWE with a thinner separator than usual could achieve greater efficiency than PEM electrolysis [22].

The Imperial College of London also performed a study in 2017 [19], comparing the current characteristics of these technologies and presented an expert point of view on future capital cost, lifetime, and efficiency of them. Most of the experts believed that AWE seems to be the strongest technology concerning the three parameters studied for now. PEM exhibits superior characteristics but requires more manufacturing and operational experience. They expect, though, that soon, sometime around 2030, PEM technology will surpass AWE technology.

Felgenhauer et al. [23] presented a comparison between sixteen different models developed by different companies. They analyzed AWE and PEM technologies regarding the economic aspects of scale, production capacity, and all costs related to the production of $H_2$. They conclude that, among the 16 electrolyzers, PEM had a slight advantage in terms of efficiency, 57 - 64 $\%_{LHV}$ compared to AW electrolyzers, 52 – 62 $\%_{LHV}$, but suffer from higher efficiency degradation. They also concluded an increase in the systems' cost-efficiency with the increase in the system capacity, which indicates that scale economies are applied. Therefore, currently, the AWE technology is the more mature and cost-efficient solution. The lower costs associated with this technology compensate for the slightly better efficiency of PEM.

In conclusion, for large-scale industrial water electrolysis, alkaline water electrolyzers seem to be more suitable: the system shows more durability and lower capital costs. Nevertheless, there are still issues to be worked out towards the efficiency of the method. That being said, the AWE technology will be discussed next, in Chapter 2.2, starting with the most important thermodynamic considerations, and followed by a review on the current advances of AWE, focusing on the principal characteristics of the cell components and cell configurations.

## 2.2 ALKALINE WATER ELECTROLYSIS

### 2.2.1 THERMODYNAMIC CONSIDERATIONS

The decomposition of water into hydrogen and oxygen is not thermodynamically favorable. To accomplish it, it is necessary to overcome an equilibrium cell voltage ($E^e_{cell}$). The equilibrium or reversible cell potential is the difference between the equilibrium potentials of the respective anode and cathode, described by Equation (8).

$$E^e_{cell} = E^e_{anode} - E^e_{cathode} \tag{8}$$

The equilibrium potential is related to the Gibbs free energy change of the overall cell reaction ($\Delta G$), by Equation (9):

$$\Delta G_{cell} = nFE^e_{cell} \tag{9}$$

where $n$ is the number of moles of electrons transferred in the reaction and $F$ is the Faraday constant. For a reaction to be spontaneous, $\Delta G_{cell}$, obtained by Equation (10), must be a negative value.

$$\Delta G_{cell} = \Delta H_{cell} - T\Delta S_{cell} \tag{10}$$

where $\Delta H_{cell}$ and $\Delta S_{cell}$ are the enthalpy change and entropy change associated with the cell reaction, respectively, and $T$ is the temperature [17].

Under standard conditions (ambient temperature of 25ºC and atmospheric pressure) the $\Delta H_{cell}$ is +286 kJ/mol of $H_2$ and the $\Delta G_{cell}$ is +238 kJ/mol of $H_2$. The difference between the two values arises because the electrolysis leads to a change from liquid to gaseous phase and hence to a large increase in the system's entropy. Then, the reversible cell potential at these conditions is 1.23 V ($\Delta G_{cell}/nF$).

When the system is isolated, the system's entropy increase cannot be achieved by absorption of the heat from the surrounding, so all the energy has to come from an electrical source, which means that it is necessary to apply a higher potential difference. The total electrical energy required for maintaining an electrochemical reaction without generation or absorption of heat at a specific temperature is called the total thermoneutral voltage ($E_{Tn}$). At standard conditions, the thermoneutral voltage is 1.48 V ($\Delta H_{cell}/nF$).

When operating away from standard conditions, the equilibrium cell potential must be calculated from the Nernst equations for the two electrode reactions leading to Equation (11),

$$E_{cell}^{e} = E_{cell}^{o} + \frac{RT}{nF} \ln \frac{a_{H_2}^2 a_{O_2}}{a_{H_2O}^2} \quad (11)$$

where $E_{cell}^{o}$ is the equilibrium potential at standard conditions, $a$ are the activities of the reactant and products and $R$ the gas constant.

Apart from the theoretical energy consumption during electrolysis, there are a number of additional electrical barriers that need to be overcome for the electrolysis process to occur. These barriers constitute the overpotential ($\eta$), which can be defined as the additional energy required, above the equilibrium potential, to drive the reaction at a desired rate – Equation (12) [17,24].

$$\eta = E - E^{e} \quad (12)$$

The overpotential is divided into three major categories: ohmic overpotential ($\eta_o$), concentration overpotential ($\eta_c$) and activation overpotential ($\eta_a$) – Equation (13) [25].

$$\eta = \eta_o + \eta_c + \eta_a \quad (13)$$

The ohmic overpotential, also called ohmic losses or potential drop, is related to the ohmic internal resistance ($R_{cell}$) of the cell that combines the resistances of the electrodes ($R_{anode}$ and $R_{cathode}$); the external electric circuit resistances, including wiring and connections at the anode and cathode, $R_{circuit}$; the resistance generated by the gas bubbles produced, $R_{bubbles}$ and the resistances of the membrane ($R_{membrane}$) and electrolyte ($R_{electrolyte}$) – Equation (14).

$$R_{cell} = R_{anode} + R_{cathode} + R_{circuit} + R_{bubbles} + R_{membrane} + R_{electrolyte} \quad (14)$$

Ohmic overpotential, as its name suggests, follows Ohm's law, Equation (15),

$$\eta_o = IR_{cell} \quad (15)$$

where $I$ is the applied current. This relation indicates that the potential drop varies linearly with the applied current [24].

The concentration overpotential is caused by the concentration gradient of the reactants or products in the electrolyte on the electrode surface due to mass transport limitations as the reactions proceed. It occurs when mass transport cannot accompany the cell reaction rate [26–28].

The activation overpotential is the difference above the equilibrium potential required to overcome the activation energy of the cell reaction to produce a specified current. This overpotential is related to the electron transfer that happens at the electrode interface.

In the absence of mass transfer limitations, the relationship between the rate of reaction, i.e., current density ($j$), and the overpotential is given by the Butler-Volmer equation – Equation (16).

$$j = j_0 \left[ exp\left(\frac{-\alpha F \eta}{RT}\right) - exp\left(\frac{(1-\alpha) F \eta}{RT}\right) \right] \quad (16)$$

$j_0$ is the exchange current density, which is defined as the rate at which the reactants are transformed into the products at equilibrium and the products are regenerated as reactants, free of any limitation due to mass transfer.$\alpha$, also represented as $\alpha_c$ is the cathodic transfer coefficient, and $(1-\alpha)$ is the anodic transfer coefficient, also represented as $\alpha_a$.

For large overpotential values, the previous equation can be simplified to give the Tafel equation, Equation (17).

$$|\eta| = a + b\log|j| \tag{17}$$

Where:

$$a = -b\log j_0 \tag{18}$$

$$b = -\frac{2.3RT}{\alpha F} \tag{19}$$

b is the so-called Tafel slope, and $\alpha$ is the cathodic or anodic transfer coefficient, depending if the Tafel equation is applied to the HER or OER, respectively [17,29].

#### 2.2.1.1 HER mechanism

The hydrogen reaction in alkaline media is widely accepted as a combination of the Volmer-Tafel and Volmer-Heyrovský mechanisms. The first step is always the Volmer step, where hydrogen is adsorbed at the electrode surface (Eq. 20). After this initial step, hydrogen can be produced either by chemical desorption, where two adsorbed atoms form a hydrogen molecule - the Tafel step (Eq. 21) - or by electrochemical desorption, where another molecule attacks the adsorbed atom of hydrogen - the Heyrovský step (Eq. 22). $H_{ads}$ represents the adsorbed status of the hydrogen.

$$H_2O + e^- \rightarrow H_{ads} + OH^- \tag{20}$$

$$2H_{ads} \rightarrow H_2 \tag{21}$$

$$H_{ads} + H_2O + e^- \rightarrow H_2 + OH^- \tag{22}$$

For the HER, it is necessary to identify the rate-determining step [17]. The Tafel slope represents a diagnostic criterion for the determination of the HER mechanisms on different electrode surfaces. Assuming that Langmuir adsorption isotherm applies, a Tafel slope of 30 mV dec$^{-1}$ suggests that the mechanism proceeds through a Volmer-Tafel route, and the chemical desorption is rate-limiting, whereas a Tafel slope of 40 mV dec$^{-1}$ indicates hydrogen production via the Volmer-Heyrovský mechanism, and the electrochemical desorption is the rate-determining step. When the Tafel slope registered is 120 mV dec$^{-1}$, the rate-determining step will depend on the surface coverage of adsorbed hydrogen: at low surface coverages by $H_{ads}$, the Volmer step is considered rate-limiting, while at saturation coverage, this value is observed for both Heyrovský and Volmer reactions [30].

The overpotential for hydrogen production, $\eta_{H_2}$, is generally measured by the Tafel equation in the form of Equation (23).

$$\eta_{H_2} = a + b\log(-j) \tag{23}$$

The overpotential on the cathode is directly related to the formation of hydrogen in the surrounding area of the electrode material, which in turn is determined by the bond between hydrogen and the electrode surface. The mechanism for hydrogen adsorption and desorption requires a good binding of hydrogen to the reaction site of the metal surface; thus, it depends on some physical properties of the electrodes [17], which will be discussed in section 2.2.2.1.

#### 2.2.1.2 OER mechanism

The mechanism of oxygen evolution reaction is more complex compared to the suggested for the hydrogen evolution reaction. Several pathways have been suggested were the most accepted for alkaline water electrolysis are:

$$OH^- \rightarrow OH_{ads} + e^- \tag{24}$$

$$OH^- + OH_{ads} \rightarrow O_{ads} + H_2O + e^- \tag{25}$$

$$O_{ads} + O_{ads} \rightarrow O_2 \tag{26}$$

where the rate-determining step is one of the charge transfer steps - Equation (24) and (25). The dependence of transfer coefficient, $\alpha$, and the Tafel slope variations can be used to identify the rate-determining step. For instance, a slow electron transfer step determines the reaction at low temperatures, and on the other hand, a slow recombination step controls at high temperatures on nickel electrodes (Eq. 26).

The Tafel equation generally measures the overpotential of oxygen evolution reaction in the form:

$$\eta_{O_2} = a + b\log j \tag{27}$$

OER's overpotential is more difficult to reduce than the HER's due to its complex mechanism and irreversibility. [17,24].

### 2.2.2 CELL COMPONENTS

#### 2.2.2.1 Electrode and electrocatalysts

To develop a proper electrode for an alkaline water electrolyzer, the materials selected must have high corrosion resistance, high conductivity, high surface area, high catalytic effect, and must have a reasonable price and lifetime [17].

To increase the efficiency of an electrolysis system, it is necessary to reduce the activation overpotentials for the hydrogen and oxygen evolution reactions [24]. This can be achieved by using

electrocatalysts on the surface of the electrodes or as the electrodes themselves. Electrocatalysts provide low activation pathways for a specific electrochemical reaction and permit the reactions to occur at high current densities. They work by changing the reaction's kinetics or even by changing the mechanisms through which the reaction takes place [20,31].

The performance of the electrodes depends not only on the composition of the catalyst but also on its surface area and microstructure [32]. When the electrolysis process occurs, hydrogen and oxygen bubbles are formed on the electrodes' surfaces, detaching themselves from the surface only when they achieve a certain size. This phenomenon decreases the electrodes' effective active area; the bubbles act as an electric shield, increasing the ohmic loss of the system [17,33]. Consequently, regarding the composition of the electrodes, in addition to having a proper catalytic activity, they must also be porous, allowing multiple pathways for electrolyte penetration [34] and facilitating the detachment of the bubbles [13]; this detachment also depends on the electrode wettability, so that hydrophilic electrode surfaces reduce the surface coverage by gas bubbles [17].

Noble metals, in particular platinum (Pt) group metals and ruthenium (Ru) and iridium (Ir), have been regarded as the benchmarked electrocatalysts for HER and OER, respectively; they are considered the most efficient electrocatalysts, with low overpotentials and low Tafel slopes. However, these noble electrocatalysts are expensive and rare, making it impossible to produce hydrogen from water splitting at a larger scale economically. Hence, scientists developed a great interest in using earth-abundant transition metals (TMs) as electrocatalysts for AWE, like nickel (Ni), cobalt (Co), iron (Fe), molybdenum (Mo), zinc (Zn), and others. Among these, Ni is the most active non-noble metal; it is stable in strong alkaline solutions and abundant and, therefore, it is a cheap material. For these reasons, Ni and Ni-based alloys are considered the principal electrocatalysts for HER and OER currently [20,32,35].

Bare Ni was once used as electrode support with a function of electrocatalyst by many researchers for the HER. However, at the current densities desired for current water electrolyzers, the overpotential for HER with Ni electrodes is reported to be about 300 to 400 mV [32], which is far too large for modern electrolyzers. Also, most of the literature reports an increase of the overpotential over time due to deactivation of the material [32,35]. Consequently, research evolved to find new pathways to activate this material and increase its catalytic performance.

Coli et al. [36] proposed an aged Ni electrode as a cathode for the AWE. At room temperature, 30 ºC, and with a 6 M KOH, this electrode had an overpotential of 170 and 385 mV at current densities of -10 and -300 mA $cm^{-2}$, respectively. At higher temperature, 75 ºC, the overpotentials, at the same current densities were 150 and 350 mV, respectively.

An obvious way to improve the electrocatalytic performance of Ni materials is to increase their surface area by developing electrodes with high porosity. The rapid development of nanotechnology has made it possible to build nanostructures with uniform size and morphological distribution, like nano-sized Ni powders and porous nickel foams (NF) or Ni meshes. NFs and Ni meshes present a higher catalytic activity than bare nickel, thus lower overpotentials [35].

Hu et al. [37] studied NF and Ni mesh's performance as electrocatalysts for HER in a 1 M KOH electrolyte at room temperature. The NF electrode reaches an overpotential of 217 mV at a current density of -10 mA $cm^{-2}$ and a Tafel slope of 130 mV $dec^{-1}$. In contrast, the Ni mesh presented an overpotential of 275 mV, at the same current density, and the Tafel slope of 143. A foam has a higher degree of porosity than a mesh, so the result was expected. The authors also performed a stability test, where the NF presented a stable potential of around -0.4 V at a constant current density of -50 mA $cm^{-2}$ for 20 h.

The deposition of Ni on other metallic substrates is also a standard procedure done by several researchers. For instance, Siwek et al. [38] obtained 3D NF deposited onto SS via galvanostatic electrodeposition from different electrolyte concentrations. The NF with the best performance revealed an onset overpotential of 130 mV, 80 mV lower than for a Ni rod. The Tafel slope obtained was 160 mV $dec^{-1}$. The double-layer capacitance and roughness factor were also obtained, 12700 uF $cm^{-2}$ and 635, respectively. In addition, a stability test was performed. The electrode presented a constant current density of about -100 mA $cm^{-2}$ for almost 4 h when subjected to a potential of -0.35 V.

In Table 2, a summary of the principal features of the electrocatalysts for HER that were described is presented.

**Table 2 – An overview of the overpotentials and Tafel slope of HER for the Ni electrodes found in the literature.**

| Electrode | Electrolyte | T / ºC | $j$ / mA $cm^{-2}$ | $\eta_{HER}$ / mV | Tafel slope / mV $dec^{-1}$ | Stability | Ref. |
|---|---|---|---|---|---|---|---|
| **Pt/C** | 1 M KOH | RT | 10 | 33 | 30 | - | [39] |
| **Aged Ni** | 6 M KOH | 30 | -10 | 170 | - | - | [36] |
| **Aged Ni** | 6 M KOH | 30 | -300 | 385 | - | - | [36] |
| **Aged Ni** | 6 M KOH | 75 | -10 | 150 | - | - | [36] |
| **Aged Ni** | 6 M KOH | 75 | -300 | 350 | - | - | [36] |
| **NF** | 1 M KOH | RT | -10 | 217 | 130 | Stable $E$ of ca. -400 mV at -50 mA $cm^{-2}$ for 20 h. | [37] |
| **Ni mesh** | 1 M KOH | RT | -10 | 275 | 143 | - | [37] |
| **Ni** | 8 M KOH | RT | onset | 210 | 98 | Stable $j$ of ca. -17.5 mA $cm^{-2}$ at -350 mV for almost 4 h. | [38] |
| **NF@SS1** | 8 M KOH | RT | onset | 190 | 100 | Stable $j$ of ca. -70 mA $cm^{-2}$ at -350 mV for almost 4 h. | [38] |
| **NF@SS2** | 8 M KOH | RT | onset | 150 | 105 | Stable $j$ of ca. -175 mA $cm^{-2}$ at -350 mV for almost 4 h. | [38] |
| **NF@SS3** | 8 M KOH | RT | onset | 130 | 160 | Stable $j$ of ca. -130 mA $cm^{-2}$ at -350 mV for almost 4 h. | [38] |

Regarding OER, metallic Ni presents insufficient catalytic activity. Ni electrodes show poor stability and overpotentials around 400 mV (at 10 mA $cm^{-2}$), as can be seen from the work of Ou et al. [40]. In the same study, the authors suggested the deposition of nickel oxide (NiO) into the Ni electrode, which reduced the overpotential by almost 110 mV. Ni in the form of oxide or (oxy)hydroxide is more stable at positive potentials than Ni in its metallic form [41]. However, the overpotential reached is still too high. To lower the overpotential, extensive efforts have been made to develop Ni alloys. In this regard, stainless steel (SS) as the alloy of Fe, Ni, chromium (Cr), and other metals is found to be a suitable candidate as an efficient electrocatalyst for water oxidation. In addition, it is an inexpensive and corrosion-resistant material with excellent mechanical strength [42].

Yu et al. [42] directly used commercially available 316L SS as an anode material. The electrode presented a Tafel slope of 30 mV $dec^{-1}$ and an overpotential of 370 mV to achieve a current density of 10 mA $cm^{-2}$ in a 1 M KOH solution. This behavior is comparable and can even surpass some electrocatalysts' performance already presented at the same conditions. The 316L SS electrode also exhibited high durability since the overpotential was maintained constant for 20 h (under the same current density). After 50 h of electrolysis at 10 mA $cm^{-2}$, the durability and stability were tested again, and the performance was consistent with the first test.

The performance of SS electrodes can usually be further improved upon surface modifications. For example, Coli et al. [36] studied the behavior of polished 316L SS under different current densities and temperatures in a 6 M KOH. At 30 ºC, the overpotential obtained at 300 mA $cm^{-2}$ was around 385 mV, which was relatively small compared to bare Ni and porous Ni (overpotentials of 400 and 455 mV respectively).

As already mentioned, an electrode with a higher degree of porosity usually presents a better catalytic performance. In the research work of Hu et al. [37], the authors suggest the use of a stainless steel mesh (SSM) as an anode in a 1 M KOH electrolyte. The electrode reached an overpotential of 275 mV at a current density of 10 mA $cm^{-2}$ and a Tafel slope of 70 mV $dec^{-1}$. The SSM electrode's stability presented a constant potential of 1.6 V for 20 h at a constant current density of 50 mA $cm^{-2}$.

Zhang et al. [43] activated an SSM material by a cathodization treatment. In a 1 M KOH electrolyte, the electrode exhibits an overpotential of 275 and 319 mV to achieve current densities of 10 and 100 mA $cm^{-2}$, respectively. This superior OER activity is due to the surface enrichment of Ni hydroxide/(oxy)hydroxide species and the facilitated removal of $O_2$ gas bubbles during the OER. Furthermore, although minor degradation was observed after long-term water electrolysis tests, its initial performance can be quickly regained by repeating the cathodization treatment.

In Table 3 a summary of some of the principal features of the electrocatalysts for OER that were described is presented.

**Table 3 - An overview of the overpotentials and Tafel slope of OER for the Ni and SS electrodes found in the literature.**

| Electrode | Electrolyte | T / ºC | $j$ / mA cm$^{-2}$ | $\eta_{OER}$ / mV | Tafel slope / mV dec$^{-1}$ | Stability | Ref. |
|---|---|---|---|---|---|---|---|
| **$IrO_2$** | 1 M KOH | RT | 10 | 330 | 76 | - | [44] |
| **Ni** | 1 M KOH | RT | 10 | 403 | 72 | Poor stability: decrease in the $j$ of 7 to 3 mA cm$^{-2}$ at 1.8 V for 25 h | [40] |
| **NiO@Ni** | 1 M KOH | RT | 10 | 294 | 41 | Stable $j$ of ca. 7.5 mA cm$^{-2}$ at 1.65 V for 25 h | [40] |
| **Polished 316L SS** | 6 M KOH | 30 | 10 | 295 | - | - | [36] |
| **Polished 316L SS** | 6 M KOH | 30 | 300 | 385 | - | - | [36] |
| **Polished 316L SS** | 6 M KOH | 75 | 10 | 260 | - | - | [36] |
| **Polished 316L SS** | 6 M KOH | 75 | 300 | 360 | - | - | [36] |
| **316L SS** | 1 M KOH | RT | 10 | 370 | 30 | Stable $\eta_{OER}$ during 25 h. Stable $j$ of ca. 17 mA cm$^{-2}$ at 1.63 V for 25 h | [42] |
| **SSM** | 1 M KOH | RT | 10 | 277 | 51 | Stable $E$ of 1.6 V at 50 mA cm$^{-2}$ for 20 h | [37] |
| **Cathodic activated SSM** | 1 M KOH | RT | 10 | 275 | 70 | Almost stable $E$ (variation < 10 mV) at 10 mA cm$^{-2}$ for 15 h | [43] |
| **Cathodic activated SSM** | 1 M KOH | RT | 100 | 319 | 70 | - | [43] |

#### 2.2.2.2 Electrolyte

The electrolyte in water electrolysis systems must have high ionic conductivity. The electrolyte solutions' concentration and temperature are the key variables that impact the ionic conductivity [26,45].

The electrolyte on an AWE system is usually an aqueous solution of NaOH or KOH. KOH is pricier but preferred over NaOH once its solutions have higher conductivity. An alkaline medium avoids the corrosion problems caused by acid electrolytes [17], making possible non-precious metal materials as electrodes or as an electrocatalyst, cheaper cell components, and lower energy consumption, lowering the cost of hydrogen production [36].

The established working temperatures for industrial alkaline water electrolyzers are between 60 – 90 ºC [13,19], as shown in Table 1, so research focused on finding the concentration which gives the highest ion conductivity at this operating temperature.

Brauns and Turek [46] compared the conductivity of KOH and NaOH at two different temperatures (25 and 50 ºC) and different ranges of electrolyte concentration – Figure 4. The conductivity of KOH had higher values with a concentration of electrolyte within 20 to 40 wt.%. In contrast, in the case of NaOH, the best conductivity values were achieved with an electrolyte concentration of 10 to 30 wt.%. Nevertheless, the conductivity of KOH was around 40 to 50 % higher than the conductivity of NaOH.

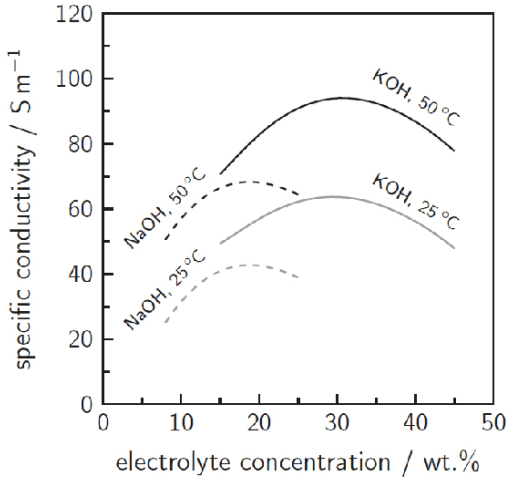


**Figure 4 - Specific electrolyte conductivity as a function of the electrolyte concentrations of NaOH and KOH solutions at two different temperatures. Adapted from [46].**

Gilliam et al. [47] used the available conductivity data for KOH to develop an equation for calculating the conductivity of KOH in the range of 0-12 M and 0-100 ºC, and with their results, Allebrod et al. [48] redrew a 3D plot of the conductivity of aqueous KOH as a function of temperature and concentration – Figure 5. In the range of the recommended temperature for alkaline water electrolyzers, the maximum conductivity values were from 20 to 40 wt.%. Other authors performed similar studies, which corroborated with these values [26,45].

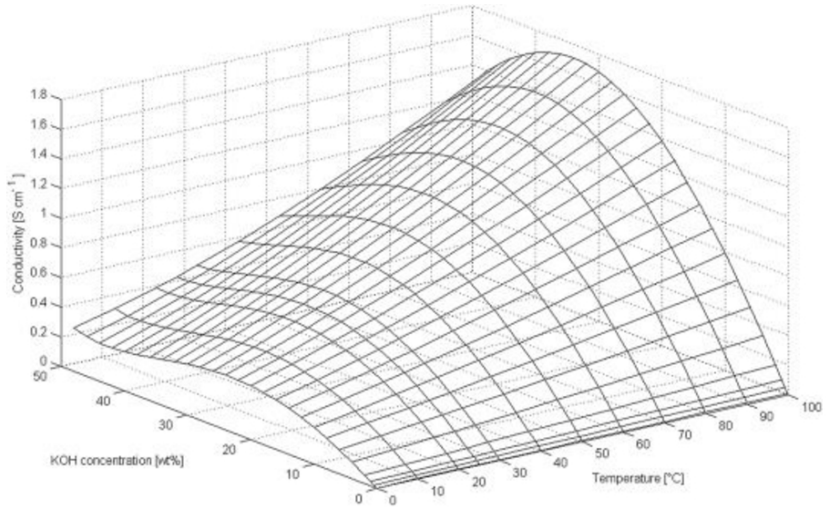


**Figure 5 - 3D plot of the conductivity of aqueous KOH solutions as a function of temperature and concentration. Adapted from [48].**

These operating conditions are the best to produce hydrogen from AWE, not only because of the electrolyte's conductivity but because of the corrosion rate. Increasing the amount of solvent leads to a more aggressive alkaline environment for the electrolyte components, contributing to increased corrosion. Rising temperatures have the same effect. So, operating with less aggressive conditions, despite the slight corrosive effect, increases the lifetime of the electrolysis components, which positively affects the total cost of hydrogen production. These temperatures also prevent a more significant water loss due to evaporation.

Efficiency loss due to gas bubbles in the electrolyte is another concern determining certain operating conditions of the electrolyte. Research indicates that applying an electrolyte flow endorse the bubble separation from the electrode surfaces during operation. Also, electrolysis cells operating at pressures around 3 MPa reduce the bubbles' volume, which minimizes the ohmic loss. However, pressurized operating environments increase the proportions of the dissolved gas and require a more endurable diaphragm [20,24].

#### 2.2.2.3 Diaphragm

The principal purpose of the diaphragm is to separate the cathode of the anode. It prevents the gases produced at the electrodes from mixing, maintaining chemical stability and safety; side redox reaction that can occur (i.e., involving reduction of a species at the cathode followed by its reoxidation at the anode), improving the efficiency of the desired reactions; and possible physical contact between the anode and the cathode if they are closely spaced. Using a diaphragm increases the cost and complexity of the cell construction and the cell potential required for a given current density because of the higher cell resistance [17].

The diaphragm material must be chemical and mechanically stable to the electrolysis media; have high selectivity for a single type of ion, high ionic conductivity, and low gas permeability; have the ability to operate efficiently at high current densities; and is better to be easy to handle, relatively low cost and have a long lifetime [17,49].

The first membranes used in commercial alkaline water electrolyzers were made from asbestos. This type of membrane had low corrosion resistance to alkaline medium at high temperatures. Due to its toxicity, it could cause serious adverse health effects, so there was the need to replace it with other materials [17,50]. Eventually, using asbestos as a diaphragm material was prohibited, and composite materials based on microporous polymers or ceramics, such as polyphenylene sulfide (PPS) and polysulphone (PSF), were found to be a good alternative [18,50]. The most popular material used as a separator is a PSF matrix with zirconium oxide as a filter, known as Zirfon [49,51,52].

### 2.2.3 CELL CONFIGURATION

The way that the electrodes and diaphragm are assembled in an electrolysis cell must also be addressed. The interelectrode distance is related to the ohmic resistance. In general, the ohmic resistance decreases with the decrease of the interelectrode distance. Hence, the electrolysis efficiency increases with the decrease of the distance between the electrodes and diaphragm [26,45].

The electrodes and the diaphragm can be assembled in a non-zero gap or zero-gap configuration - Figure 6a and 6b, respectively. For the non-zero gap structure, the electrodes are placed a few millimeters away from the diaphragm. The gases produced gather around at the small portion of the electrolyte, while they flow to the gas collectors. As already said, the increase of the concentration of gas bubbles around the electrodes increases the ohmic overpotentials, and in consequence, the electrolysis efficiency decreases. The zero-gap configuration was designed to minimize this problem. The zero-gap cell design works by compressing two porous electrodes on either side of the gas separator, forming the so-called MEA. This allows the inter-electrode gap to be as small as the diaphragm's thickness, thus significantly reducing the ohmic resistance contribution from the electrolyte between the two electrodes. Employing porous electrodes rather than solid metal plates forces the bubbles to be released from the electrodes' backside, instead of migrating towards the top of the cell, reducing their contribution to the cell voltage. In sum, the zero-gap cell design allows a minimal inter-electrode gap, compact design, and high efficiency with a higher safety degree [53].

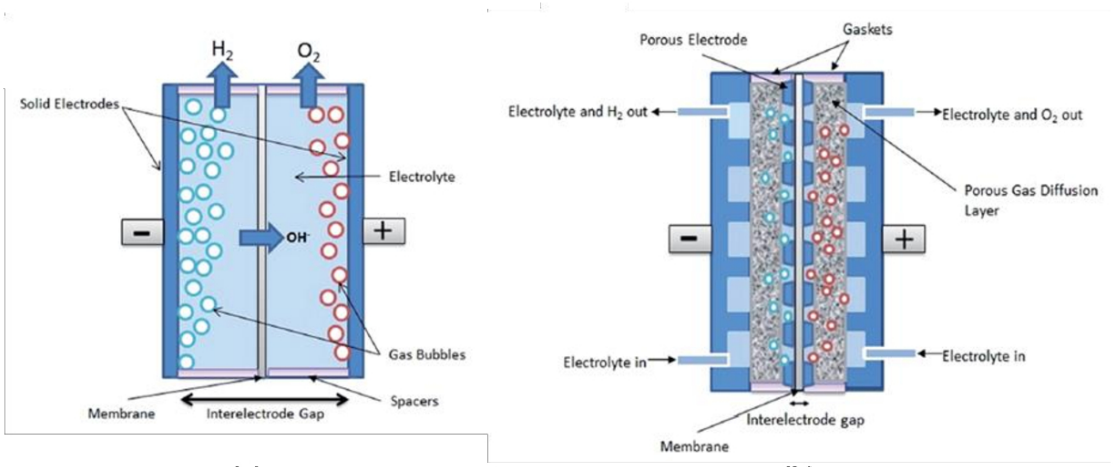


**Figure 6 - (a) Standard non-zero gap cell configuration and (b) Zero-gap cell configuration. Adapted from [53].**

### 2.2.4 ELECTROLYZER DESIGN

Industrial electrolyzers are composed of multiple electrolysis cells in a unipolar (also called tank-type) – Figure 7a – or bipolar (also called filter press) design – Figure 7b [54].

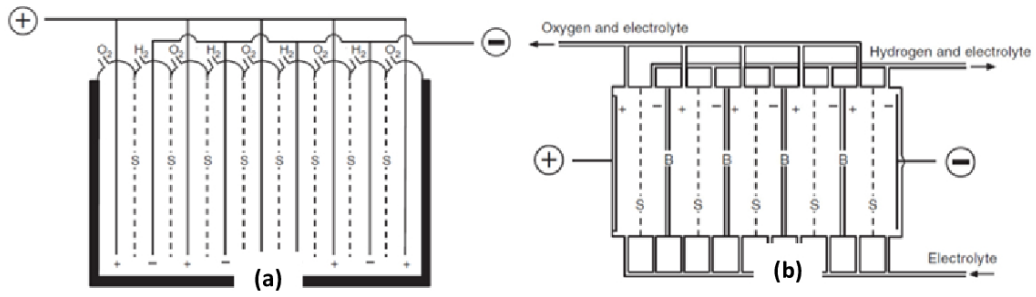


**Figure 7 - Electrolyzer module with an (a) unipolar configuration and a (b) bipolar configuration. Adapted from [17].**

In an electrolyzer with a unipolar design, positive and negative electrodes are connected alternatively in parallel and held apart by porous separators, sharing a common electrolyte. Thus, the total voltage applied to the whole electrolysis cell is the sum of of the voltage applied to the individual electrolysis cells. For typically industrial processes, the unipolar configuration presents a cell voltage of about 2.2 V. In this configuration, the same electrochemical reaction, either HER or OER, occurs on both sides of each electrode [17]. Tank type designs offer the advantages of simpler construction and maintenance, common electrolyte with no shunt currents and ease to control its concentration, no electrical contact surfaces within the cell, lower material cost, and high reliability. The main disadvantage of this configuration is that it requires substantial currents at certain voltage due to the large number of cells connected in parallel, causing large ohmic losses.

Regarding the bipolar design, a metal sheet (or bipole) connects electrically adjacent cells in series. The electrodes have bipolarity, since one electrode serves both as the cathode for one cell and de anode for the adjacent cell, which means that the two different reactions (HER and OER) take simultaneously on the opposite sides of each electrode, not directly connected to the power source. In this case, the total cell voltage is the sum of the individual unit cell voltages, which translates for a value of $2.2 \times (n - 1)$ V (where $n$ is the number of electrodes). The significant advantage of the filter press configuration is that do not require external busbars to connect individual cells. Also, the modules occupy a smaller volume for a given hydrogen output. It requires lower current and higher voltages, simplifying the power conditioning and controls. However, this design is more sophisticated, which increases the manufacturing cost [17,54].

## 2.3 HYDROGEN STORAGE

It is a well-known fact that proper and efficient storage of hydrogen is a challenge. It has been a central topic in the whole issue of implementing a hydrogen economy and the subject of several studies [55–

62] to improve all the related technology. Hydrogen storage plays a big part in the efficiency of the entire hydrogen production process. To accomplish this new energy system, mobile and stationary hydrogen storage technologies must thrive.

Both mobile and stationary storage systems have their peculiar requirements and challenges. Stationary systems can function at higher temperatures and pressures than mobile ones; and concerning their size, they can be more spacious. Mobile storage technologies must fulfill a lot more requirements. The gravimetric and volumetric capacity of storage are two significant parameters that need to be considered. Gravimetric capacity refers to the quantity of hydrogen gas a given weight of storage material can generate, while volumetric capacity refers to the quantity of hydrogen gas contained in a given volume of storage material. Higher values of both parameters are desired, but if a storage tank weighs too much, the range of the vehicle will be limited; and if the storage tank is too voluminous, the luggage space will be restricted as well [55,56]. So, the objective is to create storage systems as lightweight and compact as possible. However, this is not a simple task because hydrogen has a very low density, 0.089 kg $m^{-3}$, which means that 1 kg of $H_2$ occupies, at ambient pressure and temperature, a volume of 11 $m^3$ [57].

Hydrogen can be stored in four different ways, depending on the size of the storage and application field: compressed, cryogenic, cryo-compressed or stored in a solid or liquid material. The first three ways are considered physical storage of hydrogen. Hydrogen material storage is considered a chemical storage system given that hydrogen interacts with the storage material [58].

### 2.3.1 COMPRESSED HYDROGEN STORAGE

The most established method for physical storage of hydrogen is in the form of pressurized gas. As previously stated, hydrogen has a very low density, and because of that its storage requires high pressures or extremely low temperatures. Current applications of hydrogen as a fuel require hydrogen to be pressurized up to 35 MPa or 70 MPa. Pressurizing hydrogen can decrease its energy content by 11-13 %. Due to its lightness, at high pressures, small amounts of hydrogen will leak out over time [59].

Pressure vessels are generally cylinders and, depending on the material, they can be classified as Type I to IV [58]. The most conventional and least expensive pressure vessels are type I. They are fully metallic and normally made from aluminum or steel, which makes them the heaviest, with 1.36 kg $L^{-1}$. They have a limiting pressure of 50 MPa. Type II pressure vessel construction is similar to type I but with a glass fiber composite overwrap. The manufacturing cost of these tanks is 50 % higher than the cost of the first ones as they weigh 30 - 40 % less and are capable of support higher pressures. Regarding type III, they are made of a full-composite wrap with an aluminum liner. Its use is adequate for working pressures until 45 MPa. They have a price similar to type II tanks but weight much less, about 0.34 to 0.45 kg $L^{-1}$. Finally, type IV is an all-composite pressure vessel that can withstand pressures up to 100 MPa. It is the lightest and most expensive type[59,60]. Type I and II are the most common pressure vessels used today. Although Type III and IV are lighter hydrogen storage solutions, their technology has yet to evolve so that prices become more appealing [59].

Scientists and engineers continue exploring economical and practical ways of storing large amounts of gas. One of the most effective methods, which is in a constant development, is the storage of $H_2$ in underground salt caverns. They are extremely impervious to hydrogen, even under high pressures, which prevents leakage [55]. Germany and Texas have already applied this way of storage to natural gas [60]. In Romania, some researchers are trying to apply the same technology to store hydrogen [61].

The distribution of gaseous hydrogen is made either via tube trailers of compressed $H_2$ or via gas pipelines. This is a good low-cost option to distribute hydrogen, especially if already existing natural gas pipelines can be reused for hydrogen. Nevertheless, tube trailers are the simplest method in terms of infrastructure requirements. The advantages of this method of distribution are minor hydrogen losses and lower cost in comparison with liquid hydrogen transportation which will be discussed next. However, tube trailers have low storage capacities and have limitations regarding dimensions and maximum pressures, enforced by transportation regulations [60].

### 2.3.2 LIQUEFIED HYDROGEN STORAGE

The other way of physically store hydrogen is in the form of a cryogenic liquid. Liquefying hydrogen is done at -253 $^{o}$C, so maintaining hydrogen at a such low temperature is the main challenge of cryogenic hydrogen. Owing to its low boiling point, the cooling technology required must be able to achieve very low temperatures, which means that the process of liquefying hydrogen is both time-consuming and energy-intensive. Its energy content can decrease 40 %, in comparison with the 10 % energy loss in compressed hydrogen. The low temperature requires special double-walled vessels with good insulation systems to prevent heat leakage, which can cause serious accidents. A system like this has a hydrogen lost percentage of about 0.3-3 % due to persistent boil-off [63]. On the other hand, hydrogen at this temperature has a density of 71 g $L^{-1}$, which is adequate to use in space programs [55,58].

This storage method is most often used for medium to large-scale storage and delivery. Usually, cryogenic hydrogen is transported in delivery trucks and ships. Typically, a cryogenic tanker can carry up to 5000 kg of hydrogen, which is about five times the capacity of compressed hydrogen gas tube trailers [60].

### 2.3.3 CRYO-COMPRESSED HYDROGEN STORAGE

This method of storage was developed to be able to store hydrogen in an insulated tank that can withstand cryogenic temperatures and high pressures (at least 30 MPa) at ambient temperature. The tank consists of type III composite pressure vessel with a metallic liner that is encapsulated in a secondary insulated jacket, whose role is to limit heat transfer between the hydrogen and the environment. Cryo-compressed hydrogen storage was designed to minimize the boil-off loss from liquefied hydrogen storage while retaining a higher system energy density of 80 g $L^{-1}$ (about 10 g $L^{-1}$ higher than cryogenic storage) [58].

Hydrogen in cryo-compressed vessels can be in a liquid or compressed state, in a two-phase region (saturated liquid and vapor), but it is more economical to fill the tank with compressed gas instead of liquefied hydrogen [58]. It offers quick and efficient refueling with no need for transient flow rate control or communication between refueling stations and vehicles [62].

### 2.3.4 MATERIAL-BASED HYDROGEN STORAGE

Recently, solid-state storage systems are being considered a better long-term solution to address the safety issues that the traditional systems present, as well as being a less bulky way to store hydrogen. In this system, hydrogen is stored at a much lower pressure when compared with compressed hydrogen tanks, making the system safer since hydrogen gas leakage cannot be spontaneous and the content of the tank cannot blow up by itself. Solid-state materials can reversibly absorb and release hydrogen which is considered an advantage since they are not used up straight off [55].

Depending on the material, the storage system is based on physical sorption as in the case of porous materials or chemical sorption as in the case of hydrides (metal, complex or liquid chemical hydrides).

In porous materials, such as zeolites, porous carbon structures and metal-organic frameworks, hydrogen is adsorbed on the surface of the pores by van der Waals forces. Because this process involves weaker binding energy, it is easier to handle than chemisorption. Besides, it is reversible; when it is required, hydrogen is liberated by thermal simulation or by any other suitable technique. Hydrogen capacity is based on the surface area and pore volume of the material, and on the working pressure and temperature. Hence, this method provides low hydrogen biding energy, high surface area, faster kinetics in charge and discharge processes, and low-cost materials. These solid materials have acceptable hydrogen capacities at cryogenic temperatures of about -196 $^{o}$C and high pressures, however, these capacities at ambient temperature are less than 1 wt.%, which calls into attention the economic feasibility of storing hydrogen based on physisorption [55,60,64].

Regarding chemisorption, it involves stronger binding energy than physisorption, since molecules are dissociated on the surface of the material and then its atoms diffuse into the metal host, forming hydrides. Their reversibility conditions are very high in terms of pressure and temperature, which is a disadvantage when compared to physical sorption [58,64]. Among the hydrides, metal hydrides have been recognized as one of the most feasible solutions to store hydrogen. $MgH_2$ is considered one of the best candidates to store hydrogen onboard, since it has a high gravimetric capacity of 7.6 wt.% and the raw material is one of the least expensive. However, releasing hydrogen from these hydrides requires high temperatures, meaning that the resulting hydride is therefore expensive. Another big issue of this storage method is the weight of the materials. Tanks made of metal hydrides are heavier when compared with cryogenic liquid and compressed gas tanks. To stationary and other small storage applications this is not a problem, and with the constant research on new lighter materials, this storage method will certainly be soon incorporated in many more applications, especially in mobile ones [55,65]. In contrast to the classical metal hydrides, where interstitial sites are occupied with hydrogen atoms, in complex hydrides, hydrogen and the metal host are covalently bounded to form a complex anion. Boron hydrides like $NaBH_4$ and $LiBH_4$ have high theoretical gravimetric capacities of 10,6 wt.% and 18.4 wt.%

[58], but suffer from the disadvantage that volatile boranes are possible decomposition products, and could lead to substantial loss of storage capacity over many cycles and to damage the fuel cells. That being sad, the most studied complex hydride is $NaAlH_4$, with a reversible hydrogen content of 5.6 wt.%, once it requires lower temperatures than the boron hydrides mentioned and don't have the disadvantages presented for them. Complex hydrides had not been seriously considered as hydrogen storage materials in comparison with traditional metal hydrides, as they could effectively not be dehydrogenated unless very harsh conditions were used [65].

In the above discussion, the focus was mainly on solid materials while it is worth mentioning liquid chemical hydrides, known as Liquid Organic Hydrogen Carries (LOHCs), which show several properties similar to those of crude oil-based liquids. They can be used in ambient conditions and they are inexpensive, safe and easy to handle. Moreover, they allow long-term energy storage without hydrogen losses, like boil-off ones, and they offer less complicated ways of transporting hydrogen [63]. Besides, these carriers are not toxic or corrosive and they are not consumed, which means that they can be used repeatedly. Hydrogen is stored by chemical bonding with hydrogen-lean molecules and it is released by going through a catalyst dehydrogenation. These processes are carbon-free. However, the maximum storage capacity of these liquid carriers is 7.2 wt.%, which will limit the application of LOHCs [60].

The challenge with material-based storage of hydrogen is to be able to store hydrogen with acceptable storage density at ambient temperature, so several strategies are being evaluated. For porous materials-based physisorption systems, the focus is to improve hydrogen storage capacities at ambient temperature. For metal hydrides-based chemisorption systems, the focus is on improving the kinetics and thermodynamics of the investigated materials and developing new materials and catalysts that will enable the achievement of high storage capacities at significantly lower temperatures [64].

# 3 STUDY OF THE PERFORMANCE OF THE ELECTRODES

## 3.1 METHODOLOGY

### 3.1.1 ELECTROCHEMICAL TECHNIQUES

#### 3.1.1.1 Voltammetry

The voltammetry technique works by applying a given range of potentials to the working electrode, during a specific time, by establishing a scan rate. The current corresponding to each potential value is recorded throughout the test, resulting in a curve current vs. potential. There are several types of voltammetry. In the course of this work, only linear sweep voltammetry (LSV) and cyclic voltammetry (CV) will be addressed.

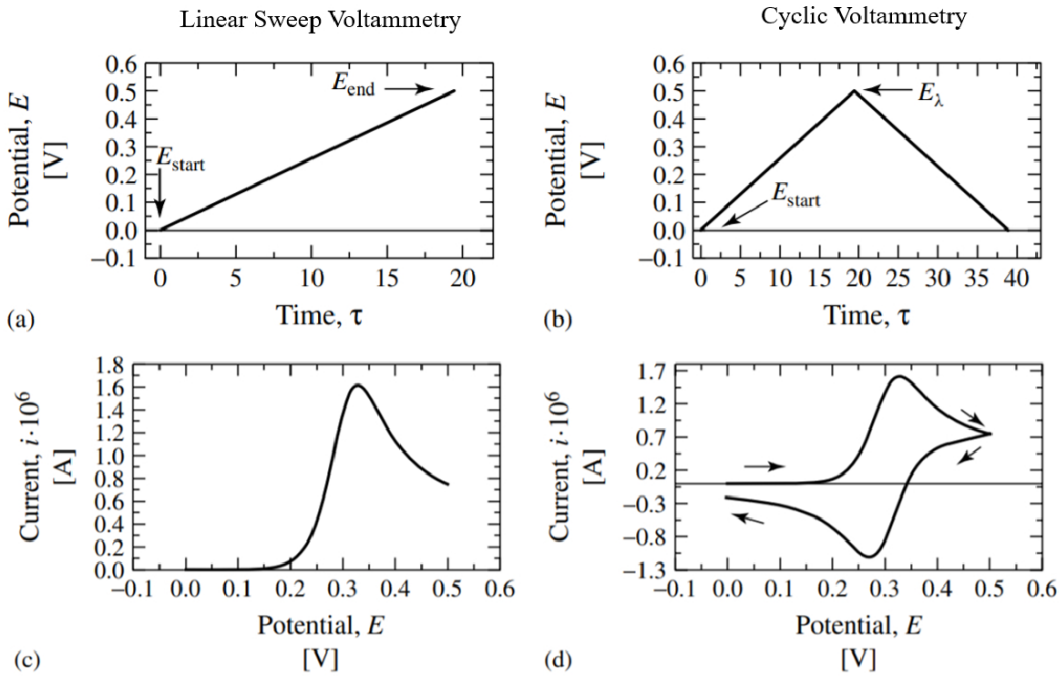


**Figure 8 – Representation of the applied potential overtime for the LSV (a) and CV (b) and the related graphic of the current vs. potential for LSV (c) and CV (d). Adapted from [67].**

Regarding LSV, the excitation signal consists of a single linear sweep from a starting ($E_{start}$) to an end ($E_{end}$) potential – Figure 8a. The resulting voltammogram is represented in Figure 8c. In this type of test, it must be used a low scan rate, so the value measured for the current be accurate. However, using a slower rate, the measurements will take lots of time. On the other hand, using faster rates, the procedure takes less time, but the measurements do not have enough time to reach the most accurate value.

The LSV technique is currently used to obtain polarization curves, a graphic representation of the current density generated at a certain potential, for the HER, OER, or the overall water electrolysis. Resorting the polarization curves of HER and OER, it is possible to do a Tafel analysis, which will be explained ahead in section 3.2.2, and conclude about the materials' performance towards these reactions.

CV is the same as LSV, with the difference that, when the sweep reaches one of the two values of limitation of the fixed range ($E_\lambda$), the scan reverse, and there is a new potential sweep in the opposite direction until it reaches the other limit value – Figure 8b. This allows the graphical representation of both anodic reaction (when going forward) and cathodic reactions (when going backward), as seen in Figure 8d [66,67].

Usually, the cyclic voltammograms are obtained to study the redox behavior of the materials. In the present work, in addition to that, the technique will also be used to obtain the double-layer capacitance of the materials to obtain the electrochemical surface area (ECSA).

#### 3.1.1.2 Chronopotentiometry

In chronopotentiometry (CP), a current is applied to the electrode. The potential changes to a value at which the flux of the electroactive species is sufficient to supply the applied current. After a specific time, the flux of redox species to the surface cannot sustain this current. The potential changes rapidly to a new value at which another species is reduced (or oxidized) [68]. With this technique, the aim is to study the capacity of a system to provide an accurate current for a given cell voltage [69].

This type of study allows taking some conclusions about the electrode's stability. If the electrode can hold the same potential over a long time, it can be said that the material presents good stability at that operational conditions.

### 3.1.2 EXPERIMENTAL SETUP AND PROCEDURE

The electrochemical experiments were done in Instituto Superior Técnico. All the electrochemical measurements were performed in a glass cell with a total volume of 100 mL, immersed in water from a thermostatic bath of J.P Selecta s.a. It was used a potentiostat/galvanostat from Admiral Instruments, controlled by the Squidstat™ Plus software.

Two different electrodes where tested: a NF (A = 9.98 $cm^2$) and a 316L SS foam (SSF) (A = 4,59 $cm^2$), from Nanoshel. The NF and the SSF performances were studied towards the HER and OER, respectively. The choice of the NF to perform as the cathode and the SSF as an anode was made by the company TecnoVeritas, before carrying out these tests. Nevertheless, the literature review presented in chapter 2.2.2.1 supports the decision.

The performance of the electrodes was studied individually in the experimental setups represented in Figure 9.

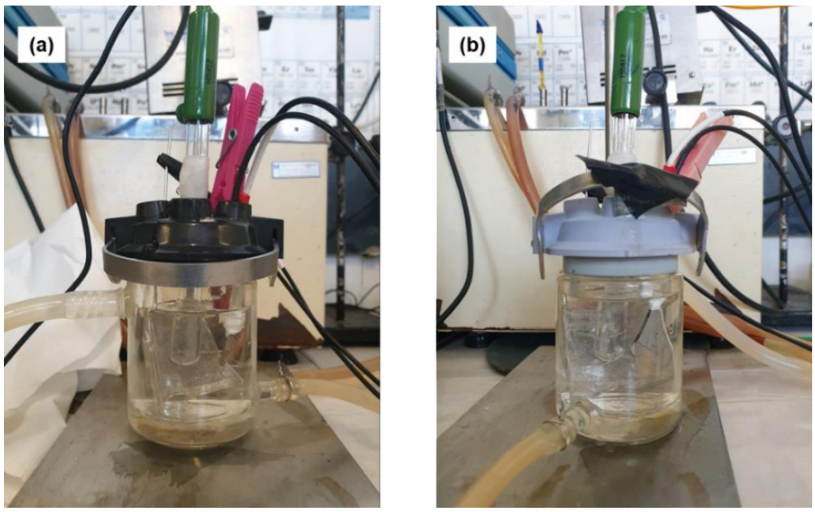


**Figure 9 - Experimental setup for studying the performance of (a) NF and (b) SSF working electrodes, a Pt mesh counter-electrode, and an SCE reference.**

The reference electrode used was a saturated calomel electrode (SCE) from HANNA Instruments, model HI5412. The CV and LSV techniques used a platinum mesh (50 $cm^2$) as a counter electrode; for the CP, a graphite electrode (4 $cm^2$). The electrolyte used for the tests was a NaOH (Eka Chemicals) solution with 10 M (30 wt.%; pH 15), prepared with Millipore water, covering 80 mL of the total volume of the cell.

Starting with the LSV, for the NF electrode, the technique was performed at different temperatures, 25, 35, 45, 55, 65, and 80 ºC, with a scan rate of 1 mV $s^{-1}$. For the SSF, it was performed at the same temperatures, at a scan rate of 2 mV $s^{-1}$.

Regarding the CV, the complete voltammograms for both electrodes were obtained at 25 ºC and 80 ºC, at the scan rates of 10, 50, and 100 mV $s^{-1}$. The electrodes were cycled 5 times at each scan rate.

To measure the electrode's capacitance, cyclic voltammograms were recorded in the non-Faradaic region of the processes (starting at the open circuit potential, OCP, and varying 50 mV around its value) at 25 ºC and different scan rates (10, 20, 30, 40, 50, 60, 70, 80, 90, 100, 200, 300, 400 and 500 mV $s^{-1}$). These tests were performed with a different electrolyte: the original electrolyte solution was diluted to a solution with 1 M NaOH (pH 14) for the NF and 0.1 M NaOH (pH 13) for the SSF. The electrodes were cycled 3 times at each scan rate.

The CP for both electrodes was performed with a constant current density of 50 mA $cm^{-2}$ (positive for the SSF electrode and negative for the NF electrode) for 16 h at room temperature.

The electrodes' performance was also evaluated towards the overall water electrolysis in the experimental setup of Figure 10, at room temperature. Here, the cathode (NF) was placed as the working electrode and the anode (SSF) as counter and reference electrode, and the potential was increased, starting at the OCP with a scan rate of 2 mV $s^{-1}$.

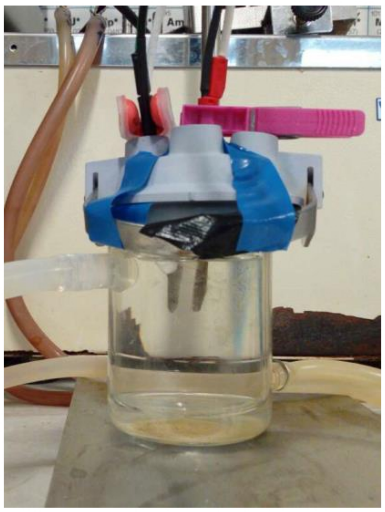

**Figure 10 – Experimental setup of the study of the performance of the electrodes towards the overall water electrolysis.**

All potentials measured against the SCE reference electrode were then converted to the reversible hydrogen electrode (RHE) scale based on Equations (28-33) depending on the solution's temperature and pH.

$$25\ ºC:\ \ E_{RHE} = E_{SCE,sat} + 0.241 + 0.059pH \quad (28)$$

$$35\ ºC:\ \ E_{RHE} = E_{SCE,sat} + 0.234 + 0.061pH \quad (29)$$

$$45\ ºC:\ \ E_{RHE} = E_{SCE,sat} + 0.227 + 0.063pH \quad (30)$$

$$55\ ºC:\ \ E_{RHE} = E_{SCE,sat} + 0.220 + 0.065pH \quad (31)$$

$$65\ ºC:\ \ E_{RHE} = E_{SCE,sat} + 0.212 + 0.067pH \quad (32)$$

$$80\ ºC:\ \ E_{RHE} = E_{SCE,sat} + 0.199 + 0.070pH \quad (33)$$

## 3.2 RESULTS AND DISCUSSION

### 3.2.1 CHARACTERIZATION OF THE REDOX BEHAVIOR OF THE ELECTRODES

#### 3.2.1.1 Ni foam

The NF's full cyclic voltammograms (fifth cycle) obtained for the different scan rates of 10, 50, and 100 mV $s^{-1}$, at 25 and 80 ºC, are represented in Figures 11a and 11b, respectively.

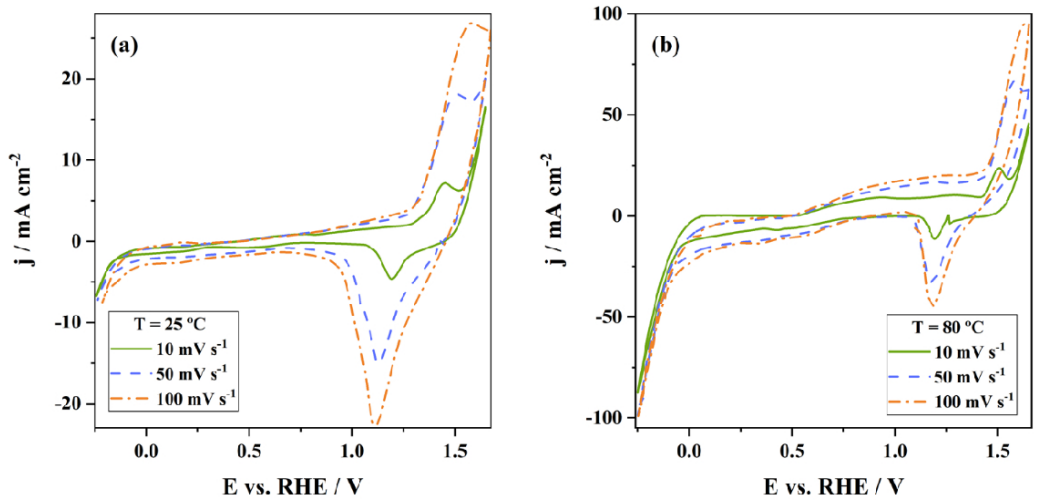


**Figure 11 - Cyclic voltammograms of the tested NF at different scan rates at (a) 25 ºC and (b) 80 ºC.**

At a higher temperature, the current densities reached by the NF are higher, which may be indicative that the temperature rise may favor the hydrogen evolution reaction. This result supports the idea already mentioned in the literature that nickel is a suitable electrocatalyst for this reaction.

At both CVs, the cathodic and anodic peaks are not at the same potentials at the different scan rates. It is possible to observe an evident increase in the oxidation peaks potential and a decrease in the reduction peaks potential, when increasing the scan rates. According to Hall [70], the first oxidation peak of Ni materials is usually observed at a potential around 0.3 V. It corresponds to the oxidation of metallic Ni to $NiO_x$ and $Ni(OH)_2$. The author recorded the CVs of polished Ni electrodes at a scan rate of 100 mV $s^{-1}$ in a 0.1 M KOH electrolyte, between the OCP and -600 mV and +500 mV vs. RHE (Figure 12) and identified the oxidation and reduction processes of the material.

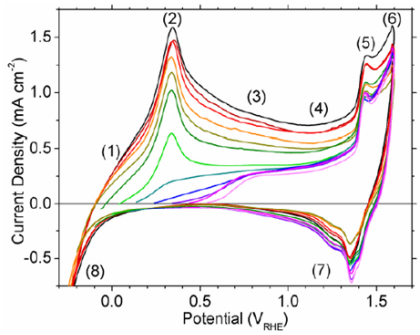


**(1)** H incorporated in the metallic Ni oxidizes and dissolves into solution
**(2)** Metallic Ni oxidizes to $NiO_x$ and α-$Ni(OH)_2$
**(3)** H incorporated in the metallic Ni oxidizes and dissolves into solution
**(4)** β-$Ni(OH)_2$ forms electrochemically and/or aging of α-$Ni(OH)_2$
**(5)** α/β-$Ni(OH)_2$ oxidize to β-NiOOH
**(6)** $H_2O/OH^-$ oxidize to $O_2$ - OER
**(7)** β-NiOOH reduces to β-$Ni(OH)_2$
**(8)** β-$Ni(OH)_2$, $NiO_x$ and α-$Ni(OH)_2$ reduce to metallic Ni / $H_2O$ reduces to $H_2$ - HER

**Figure 12 – Cyclic voltammogram of a freshly polished Ni electrode recorded at a scan rate of 100 mV $s^{-1}$ at room temperature, in a 0.1 M KOH electrolyte. Adapted from [70].**

In the complete CV at 25 ºC, the first peak is ill-defined at around 0.30 V. At 80 ºC, the peak is a bit deviated from this potential, it starts to appear at around 0.7 V.

A new oxidation process, corresponding to the oxidation of the $Ni(OH)_2$ to NiOOH, is observed. At 25 ºC, this peak occurs at potentials of 1.45 V and 1.55 V. At 80 ºC, the potentials where the peak appears variate between 1.50 and 1.60 V. At higher scan rates, the distinction between that peak and the next anodic process, corresponding to the OER, becomes less noticeable. In the work of Hall, this peak appears at a potential of 1.45 V [70], which is close to the result achieved in the CVs for both temperatures, especially for 25 ºC.

The last oxidation process observed corresponds to the OER (oxidation of $H_2O/OH^-$ to $O_2$), as mentioned in the paragraph above. For both temperatures, it is observed that the production of oxygen starts at a potential of around 1.55 – 1.65 V.

In respect to the cathodic processes, at 25 ºC, the first reduction peak happens at a potential around 1.20 V, at the scan rate of 10 mV $s^{-1}$, undergoing a shift to lower potentials at higher scan rates, to the potentials of 1.15 and 1.10 V for the scan rates of 50 and 100 mV $s^{-1}$. At 80 ºC, the peak occurs around 1.20 V at all the scan rates.

In the CVs, there are two more reduction processes: the reduction of $Ni(OH)_2$ and $NiO_x$ to metallic Ni, followed by the curve corresponding to the reduction of $H_2O$ to $H_2$ (hydrogen evolution reaction). However, as observed in the reference [70], the first, it not easy to identify and occur right before the HER.

At the higher temperature, hydrogen production starts at a lower potential, between -0.10 and 0 V, than at ambient temperature, between -0.20 and -0.15 V, which is in accordance with the fact already announced that the temperature rise favors the HER.

All the redox processes mentioned are summarized in Table 4.

**Table 4 – Identification of the redox processes present in the cyclic voltammograms and the potential at which they occur.**

| E vs. RHE / V | | Processes |
|---|---|---|
| 25 ºC | 80 ºC | |
| 0.30 | 0.70 – 0.90 | Metallic Ni oxidizes to NiO and $Ni(OH)_2$ |
| 1.45 – 1.55 | 1.50 – 1.60 | $Ni(OH)_2$ oxidizes to NiOOH |
| 1.55 – 1.65 | 1.55 – 1.65 | $OH^-$ oxidizes to $O_2$ → OER |
| 1.10 – 1.20 | 1.17 – 1.20 | NiOOH reduces to $Ni(OH)_2$ |
| -0.15 – -0.10 | -0.10 – 0 | $Ni(OH)_2$ and NiO reduce to metallic Ni |
| -0.20 – -0.15 | -0.10 – 0 | $H_2O$ reduces to $H_2$ → HER |

Comparing the results with the literature, the current densities reached in the CVs are much higher than those presented in the literature. First, this can be explained because, in the literature, it is used as a polished electrode rather than a NF. Porous electrodes usually show a better catalytic performance, which results in higher current densities. Second, the electrolyte used in this experience has a higher concentration than the electrolyte used by Hall; therefore, greater conductivity. Also, the potentials where the oxidation and reduction processes occur were a bit different, a fact that can be related to the electrolyte diffusion limitations being more pronounced inside a thick porous network rather than in a rod surface.

### 3.2.1.2 SS foam

The complete cyclic voltammograms (fifth cycle) of the SSF obtained for the different scan rates of 10, 50, and 100 mV $s^{-1}$, at the temperatures of 25 ºC and 80 ºC, are represented in Figure 13a and 13b, respectively.

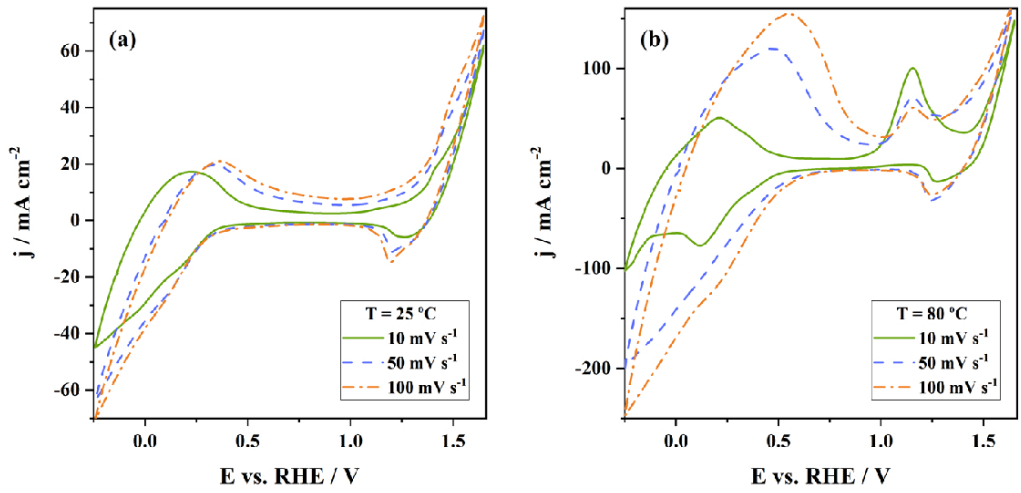


**Figure 13 - Complete cyclic voltammograms of the tested SSF at different scan rates at (a) 25 ºC and (b) 80 ºC.**

Three different regions in the voltammograms can be differentiated, especially at the temperature of 25 ºC. This division has been previously reported in the literature. As an example, Díaz et al. [71] presented the CVs of 316L SS in 0.1 M NaOH at different scan rates: 2, 5, and 10 mV $s^{-1}$ – Figure 14. The authors assign the first region to potentials lower than -0.6 V vs. SCE (0.41 V vs. RHE). This region is associated with iron activity. The main process that occur in this region is de formation of magnetite, which follows the redox equation shown in Equation (34). The following region extends to 0.2 mV vs. SCE (1.21 V vs. RHE) and corresponds to the passivity region, where the current densities are very low. Finally, at higher potentials, the authors identify the redox processes associated with low-high oxidation states of the species Cr, Ni, and Mo

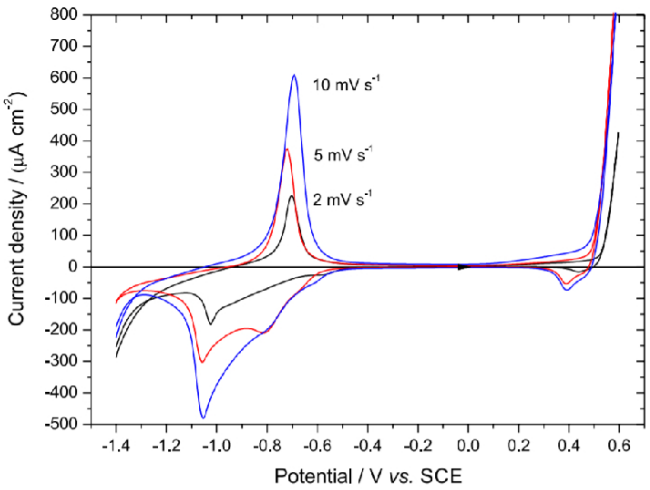


**Figure 14 - Cyclic voltammograms of a 316L electrode obtained in 0.1 M NaOH, at 2, 5, and 10 mV $s^{-1}$, at room temperature. Adapted from [71].**

$$3FeO + 2OH^- \rightleftarrows Fe_3O_4 + H_2O + 2e^- \quad (34)$$

The first process that is observed in the voltammograms is the reduction of $H_2O$ to $H_2$. Hydrogen stars to form around -0.15 V at 10 mV $s^{-1}$ and around -0.05 at 50 and 100 mV $s^{-1}$ for both temperatures.

Regarding the CV at 25 ºC, the region associated with the iron activity is located until around a potential of 0.55 V. In this region is possible to identify the oxidation process at the potentials of 0.2 V (10 mV $s^{-1}$) and 0.35 V (50 mV $s^{-1}$ and 100 mV $s^{-1}$). At 80 ºC, the same region is identified until the maximum potential of 0.50 V, 0.75 V, and 0.90 V for the scan rates of 10, 50, and 100 mV $s^{-1}$, respectively. The oxidation peak happens at the potentials of 0.15 V (10 mV $s^{-1}$), 0.45 (50 mV $s^{-1}$) and 0.60 V (100 mV $s^{-1}$). According to the literature [58], this oxidation process corresponds to the formation of magnetite, $Fe_3O_4$.

At the same region mentioned above, occurs the reduction of $Fe_3O_4$ to FeO. At 25 ºC, this reduction peak is present at a potential around 0.25 V; and at 80 ºC corresponds to a potential of 0.1 V for 10 mV $s^{-1}$ and 0.2 V for 50 and 100 mV $s^{-1}$. Contrary to what is visible in the literature's cyclic voltammogram, only one peak is identified in the present results. At higher scan rates, for both temperatures, the peak is less evident.

The second region mentioned in the literature is the passivity region. This region is easily seen at 25 ºC and extends between the end of the first region until around 1.1 V. At the higher temperature, the current densities are higher, a factor that makes it difficult to separate the three regions. Nevertheless, it is possible to associate the end of the passivity region to the potential of 1 V.

Above the previously mentioned potentials occurs the redox processes associated with the other species present in the SS 316L alloy (Ni, Cr, and Mo). It is possible to identify one oxidation peak at the CVs, at 25 ºC and 10 mV $s^{-1}$, the process is visible at 1.4 V, and for higher scan rates, the peak is close to 1.5 V. At 80 ºC, the oxidation process occurs at 1.15 V, at all scan rates. The corresponding reduction process appears around 1.2 V at 25 ºC and 1.25 V at 80 ºC, at 10 mV $s^{-1}$. For higher scan rates, the peak is slightly shifted to the left.

The last visible process is the OER. At 25 ºC, the oxygen evolution starts at a potential around 1.35 V and at 80 ºC at 1.40 V, in agreement with the work of Díaz et al. [71].

Comparing both CVs, it is clear that the current densities are higher at higher temperatures, and oxidation and reduction processes are much more evident. This can be a good indication that an increase in the temperature favors the reactions. Also, the oxygen production starts at a lower potential at 80 ºC than at 25 ºC.

Another aspect that needs to be addressed is that it was expected that the OER reached higher current densities than those obtained for HER at similar overpotential. However, this does not prevent the SS from being considered a good electrocatalyst towards the OER because the current densities recorded for the OER are equally high.

### 3.2.2 STUDY OF THE HER/OER FROM THE TAFEL ANALYSIS

#### 3.2.2.1 Ni foam

The NF electrode performance was evaluated towards the HER. The polarization curves and the Tafel plots, at the different temperatures of 35 ºC, 45 ºC, 65 ºC, and 80 ºC, are presented in Figures 15a and 15b. The measurements done at 25 ºC were omitted because they did not follow the tendency of the other temperatures.

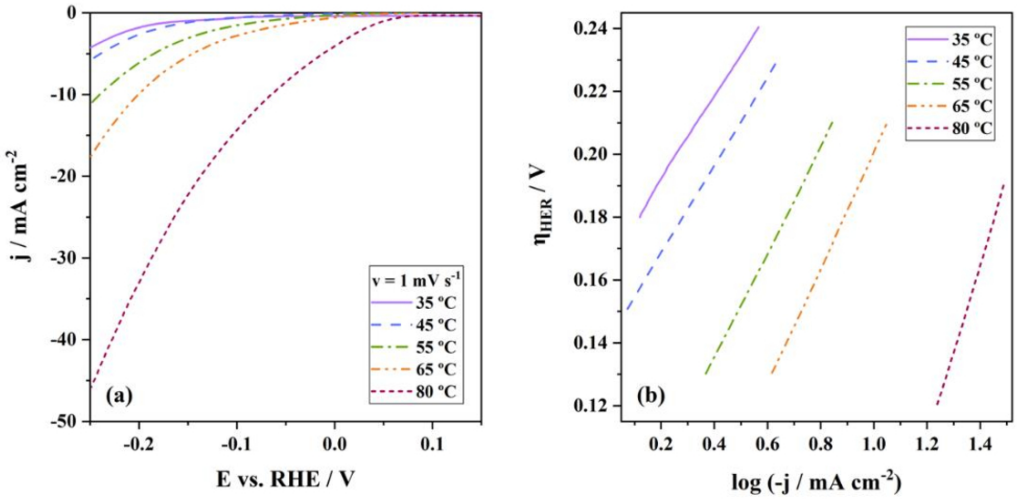


**Figure 15 - (a) Polarization curves and (b) the corresponding Tafel plots for the NF electrode at different temperatures.**

The direct observation of the polarization curves obtained at the different temperatures, Figure 15a, suggests that the temperature increase favors the hydrogen evolution. This affirmation is supported by the higher current densities (more negative) reached at higher temperatures. In addition, the HER curve starts at lower potentials when the temperature increases. The formation of $H_2$ starts at a potential between -0.25 and -0.20 V for all temperatures except 80 ºC, which starts around 0 V.

To support this statement, the Tafel plots, Figure 15b, were obtained by adjusting the experimental data to Equation (25). The overpotential was determined using Equation (12), where the reversible cell potential considered was 0 V vs. RHE. From the Tafel plots, it was possible to obtain the Tafel slope directly and calculate the cathodic charge transfer coefficient, following Equation (21) and the exchange current density, by Equation (20). All these parameters are reunited in Table 5. The onset overpotential ($\eta_{onset}$), meaning the overpotential required for the HER start, was obtained by the interception of the vertical line (that comes from the increase of the current density with the potential) and the almost horizontal line that represents the current densities close to 0.

**Table 5 - Parameters obtained for the HER at the NF electrode from the Tafel analysis.**

| T / ºC | 35 | 45 | 55 | 65 | 80 |
|---|---|---|---|---|---|
| $b$ / mV dec$^{-1}$ | 132 | 139 | 167 | 185 | 279 |
| $\alpha_c$ / V | 0.46 | 0.45 | 0.38 | 0.34 | 0.26 |
| $j_0$ / mA cm$^{-2}$ | 0.056 | 0.096 | 0.390 | 0.821 | 6.465 |
| $R^2$ | 0.999 | 1 | 0.999 | 0.999 | 0.999 |
| $\eta_{onset}$ / mV | 220 | 190 | 185 | 170 | 75 |

With respect to the Tafel slope, the values follow the tendency of increasing with the temperature. Usually, an increase in the Tafel slope with the temperature suggests that the temperature rise does not favor the reaction: the higher the Tafel slope, the smaller the current density variation for a greater potential variation. However, between 35 to 65 ºC, the observed increase in the Tafel slope is not that sharp.

The Tafel slopes recorded for the first three temperatures (35 ºC, 45 ºC and 65 ºC) are more in accordance with the ones found in the literature, presented in Table 2, section 2.2.2.1, than at the higher temperatures (65 ºC and 80 ºC). It is expected that for foam type electrodes, the parameter b assumes higher values.

Nevertheless, the work done by Pierozynski and Mikolajczyk [72] supports the results. These authors studied the temperature dependence of several parameters, including the Tafel slope, in NF in 0.1 M NaOH over the temperature range of 20 to 60 ºC. Their results, presented in Table 6, follow the same trend, increasing with the temperature.

In the HER, the Tafel slope, as already mentioned, is indicative of the reaction mechanism. Since all the values are superior to 120 mV dec$^{-1}$, it can be concluded that the rate-determining step can be either the Volmer or Heyrovsky, depending on the surface coverage of the adsorbed hydrogen.

**Table 6 – Exchange current density and Tafel slope of the HER obtained for the temperature range of 20 – 60 ºC by Pierozynski and Mikolajczyk. Adapted from [72].**

| | 20 ºC | 30 ºC | 40 ºC | 50 ºC | 60 ºC |
|---|---|---|---|---|---|
| $j_0$ / A cm$^{-2}$ | 1.2 x 10$^{-6}$ | - | - | - | 2.0 x 10$^{-5}$ |
| Tafel slope / mV dec$^{-1}$ | 137 | 169 | 183 | 193 | 222 |

It can be noticed that the $\eta_{onset}$ decreases with the increase of the temperature, suggesting that temperature favors the reaction. Their values are in accordance with the ones presented in Table 2, except at 80 ºC. At this temperature, the overpotential is exceptionally low when compared with the literature.

Regarding the exchange current density, it is clear its increase with temperature, Figure 16a, meaning that the rate of the reaction increases, supporting the idea that the rise of the temperature favors the

HER. The first two values, obtained at the temperatures of 35 ºC and 45 ºC, are in the same order of magnitude as the value presented in Table 6. For higher temperatures, the $j_0$ surpasses the information of the literature, and especially for 80 ºC, shows an outstanding result.

The activation energy, $E_a$, which represents the energy necessary to apply to the system for the reaction to take place, was also calculated using the Arrhenius equation, Equation (35). The relation between the logarithm of $j_0$ with the reciprocal temperature is present in Figure 16b.

$$\ln j_0 = \ln A_i - \frac{E_a}{RT} \tag{35}$$

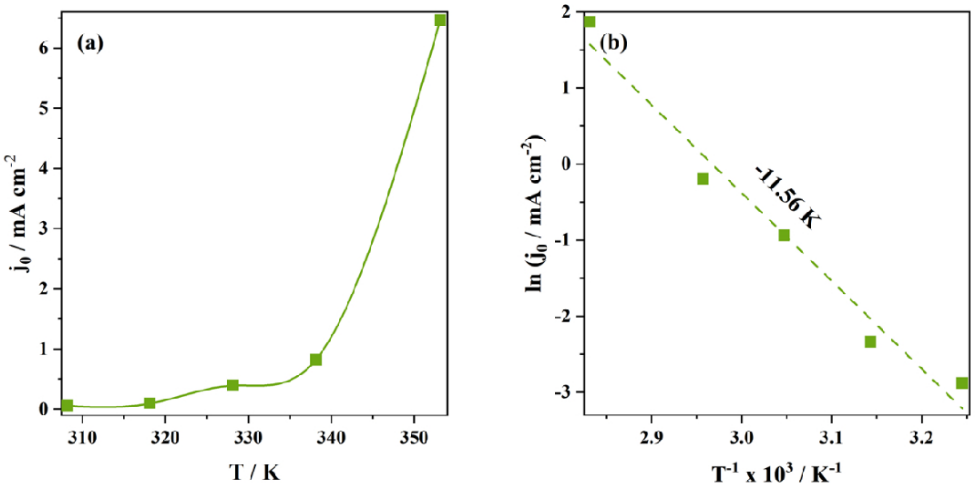


**Figure 16 – (a) Effect of the temperature on the determined $j_0$ values and (b) the corresponding Arrhenius plot (ln $j_0$ vs. $T^{-1}$) for the NF.**

The adjustment to the Arrhenius equation was acceptable, with an $R^2$ value of 0.97. The slope obtained was -11.56 K, which originated a $E_a$ of 96 kJ $mol^{-1}$. The resulting $E_a$ is superior when compared with pure Ni electrodes (51 kJ $mol^{-1}$ [73]). This result may be explained by the large increase of $j_0$ with the temperature, which led to a higher slope.

Last but not least, it is possible to see that as the temperature rises, the $\alpha_c$ value deviates slightly from 0.5. Usually, a transfer coefficient close to 0.5 translates into good reversibility of the reaction. When the cathodic transfer coefficient assumes lower values, it means that the oxidation processes are favored, and that the energy fraction that contributes to the $H_2$ production decreases. This is a negative point to the performance of the NF electrode at higher temperatures.

In conclusion, it can be said that the NF electrode shows an excellent performance towards the HER at all temperatures and that the temperature rise enhances this behavior. The less positive results obtained regarding the cathodic transfer coefficient and Tafel slopes are not sufficient to refute this statement, since the $j_0$ increase with the temperature is outstanding.

### 3.2.2.2 SS foam

As already mentioned, the SSF electrode performance was evaluated towards the OER. The polarization curves and the respective Tafel plots, at the different temperatures of 35 ºC, 45 ºC, 65 ºC, and 80 ºC, are presented in Figure 17a and 17b, respectively. The measurements done at 25 ºC are not included since they do not follow the trend of the other temperatures.

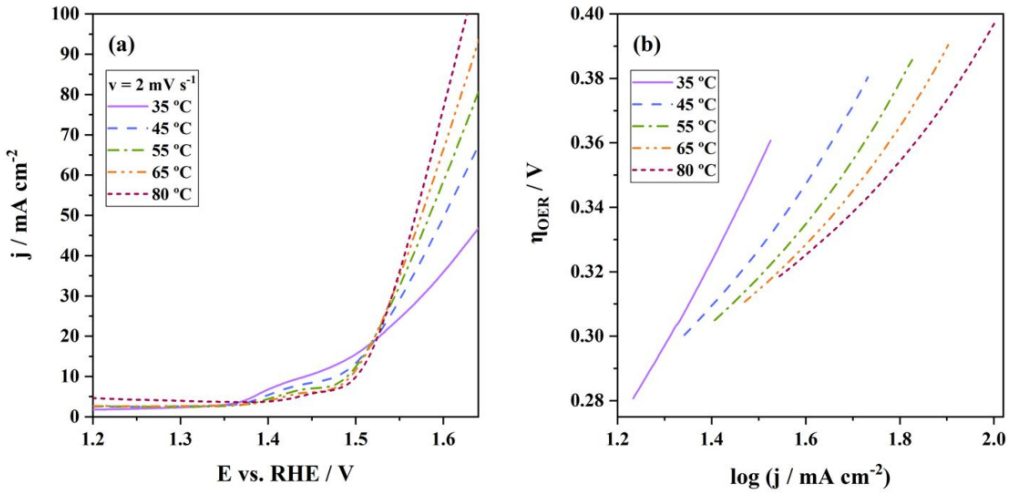


**Figure 17 – (a) Polarization curves and (b) Tafel plots for the SSF electrode at different temperatures.**

Regarding the polarization curves – Figure 17a – the current density tends to become higher with the increase in the temperature after OER starts. In general, the OER starts at a potential around 1.5 V. So, it seems that the increase of the temperature favors the oxygen evolution reaction.

It is also possible to observe an oxidation peak, more evident at lower temperatures, just before OER begins. This peak was already identified in the cyclic voltammograms of the SSF electrode, presented in section 3.2.1.2, which is a process related to the oxidation of the species of Cr, Ni, and Mo.

Regarding the Tafel plots – Figure 17b – they were obtained by adjusting the experimental data to Equation (29). The overpotential was calculated using Equation (12), where the reversible cell potential considered was 1.23 V vs. RHE. From the Tafel plots, it was possible to obtain the Tafel slope directly and calculate the anodic transfer coefficient, $\alpha_a$, Equation (21), and the exchange current density, Equation (20). All these parameters are summarized in Table 7. The onset overpotential was obtained by observing the LSV curves.

**Table 7 – Parameters obtained for the SSF electrode from the Tafel analysis.**

| T / ºC | 35 | 45 | 55 | 65 | 80 |
|---|---|---|---|---|---|
| $b$ / mV dec$^{-1}$ | 285 | 206 | 199 | 185 | 174 |
| $\alpha_a$ / V | 0.21 | 0.31 | 0.34 | 0.35 | 0.38 |
| $j_0$ / mA cm$^{-2}$ | 1.820 | 0.800 | 0.717 | 0.665 | 0.553 |
| $\eta_{onset}$ / mV | 230 | 250 | 260 | 280 | 290 |
| $R^2$ | 0.9982 | 0.993 | 0.99 | 0.9892 | 0.9872 |

Starting by analyzing the Tafel slope, the values decrease more than 100 mV with the increase of the bath's temperature. This information translates that the temperature rise contributes favorably to oxygen formation. Nevertheless, when compared with the Tafel slopes found in the literature present in Table 3, they are still higher than expected. Tafel plots reported in the literature are usually around 40 to 70 mV $dec^{-1}$, while the ones presented are superior to 170 mV $dec^{-1}$.

On the other hand, the onset overpotential increases with the temperature. Thus, this parameter allows a contrary conclusion to that obtained through the Tafel slope. Still, compared to the literature present in Table 3, the results are outstanding. The overpotentials determined at the temperatures between 35 to 55 ºC are outstanding since no previous studies presented such low overpotentials. For the temperatures of 65 and 80 ªC, the overpotentials are more in accordance with the ones found in the literature.

Regarding the exchange current density, it was impossible to find this parameter in the literature to compare with the present work. The $j_0$ values show a slight decrease with the temperature rise, which means that the rate of the reaction, i.e., the velocity of the reaction, decreases with the temperature rise. Nevertheless, the small decrease of this parameter with the temperature is a direct consequence of the values obtained from the Tafel analysis, since is quite dependent on the decrease of the Tafel slope. Therefore, it cannot be considered an indication that the temperature rise does not favors the reaction.

Finally, concerning the anodic transfer coefficient, it can be seen that its value is below 0.50 at all temperatures, which is indicative that the reduction is favored. Nevertheless, with the temperature increase, the $a_a$ also starts to increase.

Based on this analysis, the overall conclusion is that the temperature rise favors the OER. Despite the $j_0$ decrease with temperature, making impossible to obtain the activation energy for this reaction, the significant decrease of the Tafel slopes and the current densities with the temperature rise are sufficient to make this statement.

### 3.2.3 DETERMINATION OF THE ECSA

The ECSA, represents the area of the electrode material in contact with the electrolyte, where the HER and OER happen. In the case of foam electrodes, this area is not the same as the geometric area.

There are several ways to calculate the ECSA. In the present work, it will be determined as the ratio of the double-layer capacitance for the foam, $C_{dl\ foam}$ (µF), and that for the smooth electrode, $C_{dl\ smooth}$ (µF $cm^{-2}$) – Equation (36).

$$ECSA = \frac{C_{dl\ foam}}{C_{dl\ smooth}} \tag{36}$$

This method consists of cycling the electrodes at different scan rates in a non-faradaic charging process, ± 50 mV around the OCP. With the data from the CVs, it is possible to calculate the average capacitive

current, $I_{dl}$. At each scan rate. The linear slope of the average capacitive current, $I_{dl}$, as a function of the scan rate, $v$, allows calculating the double-layer capacitance, according to Equation (37),

$$I_{dl} = \frac{|I_c| + |I_a|}{2} = C_{dl}\left(\frac{dE}{dt}\right) \tag{37}$$

where $I_c$ and $I_a$ stand for the cathodic and anodic currents at the potential value in the middle of the selected potential window, respectively [38,74].

With the ECSA calculated, it is possible to obtain the roughness factor $(R_f)$ of an electrode, dividing it by the geometric area, like in Equation (38).

$$R_f = \frac{ECSA}{A_{geometric}} \tag{38}$$

#### 3.2.3.1 Ni foam

The cyclic voltammograms recorded at several scan rates are presented in Figure 18a. It is observed that the curves approach the expected rectangular behavior, confirming the existence of the double-layer capacitance. The average capacitance current of all scan rates, at the potential of 0.795 V was obtained following the expression of Eq. 39 and plotted as a function of the scan rate – Figure 18b. To ensure good linearity the $I_{dl}$ value corresponding to the scan rates of 40 and 50 mV $s^{-1}$ were ignored. The results collected are presented in Table 8.

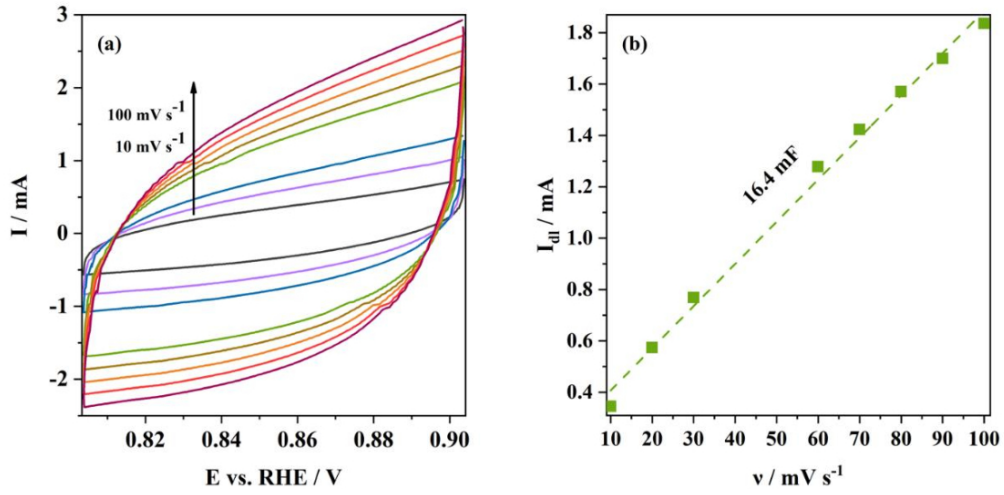


**Figure 18 – (a) Cyclic voltammogram of the NF recorded at 10, 20, 30, 60, 70, 80, 90 and 100 mV $s^{-1}$, in the potential window of -50 mV ≤ OCP ≤ +50 mV. (b) Average capacitive current, $I_{dl}$, as a function of the potential scan rates.**

**Table 8 – Double-layer capacitance and ECSA measured for the NF.**

| | |
|---|---|
| $C_{dl\ smooth\ Ni}$ / µF cm$^{-2}$ [38] | 20 |
| $C_{dl\ Ni\ foam}$ / µF | 16400 |
| ECSA / cm$^2$ | 820 |
| $R_f$ | 82 |

### 3.2.3.2 SS foam

The cyclic voltammograms obtained for the different scan rates are represented in Figure 19a. At a potential of 0.885 V, the average capacitive current was plotted against the scan rates, as shown in Figure 19b. The results collected are summarized in Table 9.

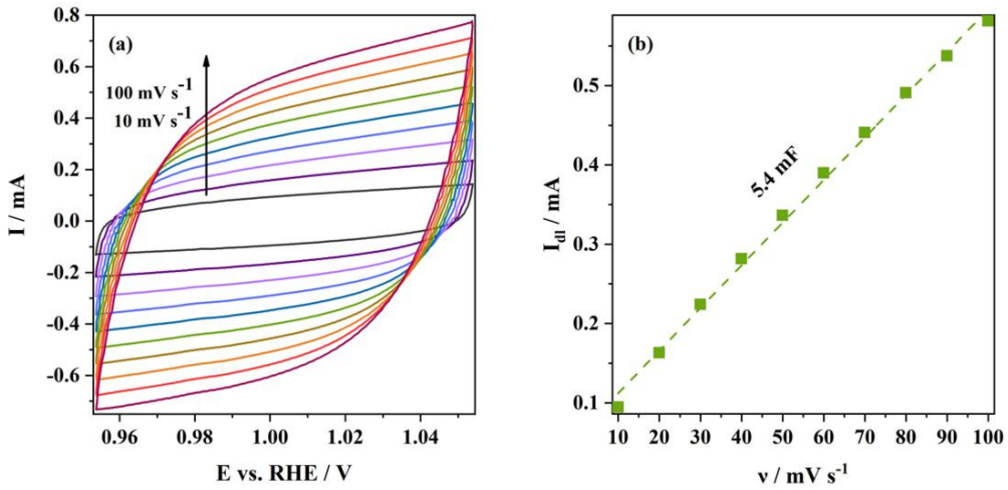


**Figure 19 – (a) Cyclic voltammogram of the NF recorded at 10, 20, 30, 40, 50, 60, 70, 80, 90 and 100 mV s$^{-1}$, in the potential window of -50 mV ≤ OCP ≤ +50 mV. (b) Average capacitive current, $I_{dl}$, as a function of the potential scan rates.**

**Table 9 - Double-layer capacitance and ECSA measured for the SS 316L foam.**

| | |
|---|---|
| $C_{dl\ smooth\ SS}$ / µF cm$^{-2}$ [71] | 30.1 |
| $C_{dl\ SS\ foam}$ / µF | 5400 |
| ECSA / cm$^2$ | 179 |
| $R_f$ | 39 |

### 3.2.4 STABILITY TEST

To evaluate the NF electrode's long-term performance and draw conclusions about its stability, the electrodes were subjected to a constant current density of 50 mA $cm^{-2}$ (in absolute value) for 16 h straight.

#### 3.2.4.1 Ni foam

The potential recorded at -50 mA $cm^{-2}$ as a function of time is represented in Figure 20.

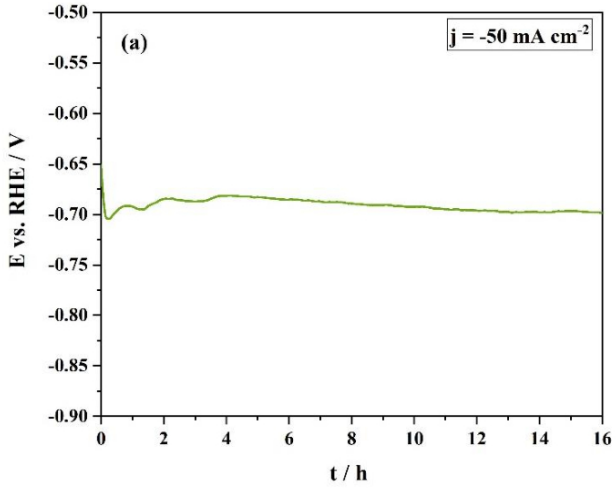


**Figure 20 – Chronopotentiometry curve for the NF electrode at a constant current density of 50 mA $cm^{-2}$ at room temperature.**

When submitted to -50 mA $cm^{-2}$, the NF presented an almost steady potential, varying only about 0.02 V the 16 h, which allows the conclusion that the electrode presents grate stability in alkaline solutions. The potential stabilizes around -0.7 V, a value a bit higher than the one obtained in reference [37], which was about -0.4 V. This deviation may be relatable with the different operational conditions that the teste was performed: the present study was made in a 10 M NaOH electrolyte, while the other was made in 1 M KOH.

### 3.2.4.2 SS foam

The chronopotentiometry curve obtained at 50 mA $cm^2$ is present in Figure 21.

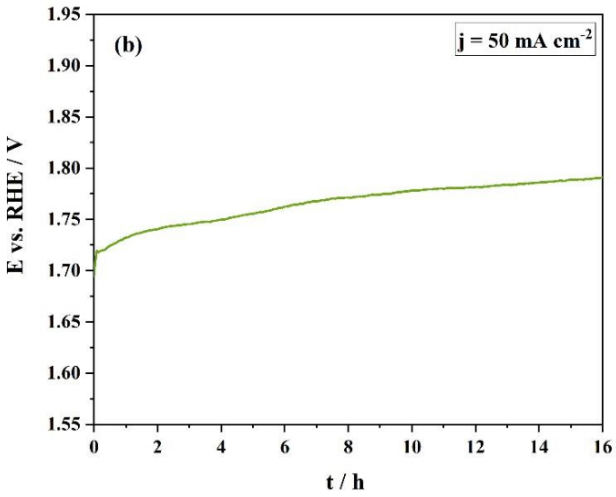


**Figure 21 - Chronopotentiometric curve for the SSF electrode at a constant current density of 50 mA $cm^{-2}$ at room temperature.**

The SSF showed acceptable stability in alkaline media when subjected to a current density of 50 mA $cm^{-2}$. The potential varies around 0.8 V within the 16 h test, stabilizing at a potential close to 1.8 V. As in the NF case, the potential reached by this electrode is also a bit higher than the one present in the reference [37], which was around 1.6 V. Being the electrode studied in the reference a mesh, rather than a foam, it was expected to obtain a lower potential. Nevertheless, just like was said, the operational conditions also influence the results.

From Figures 21 and 22 it seems that to generate a current density of 50 mA $cm^{-2}$, with NF as cathode and SSF as the anode, it is necessary to apply 2.4 – 2.5 V.

### 3.2.5 STUDY OF THE PERFORMANCE OF THE ELECTRODES TOWARDS THE OVERALL WATER ELECTROLYSIS

Based on the good results obtained for the electrodes' individual performance, it was further studied their catalytic performance for overall water splitting in a two-electrode system by using NF as cathode and SS 316L foam as the anode. It was recorded the polarization curve represented in Figure 22 at 2 mV $s^{-1}$.

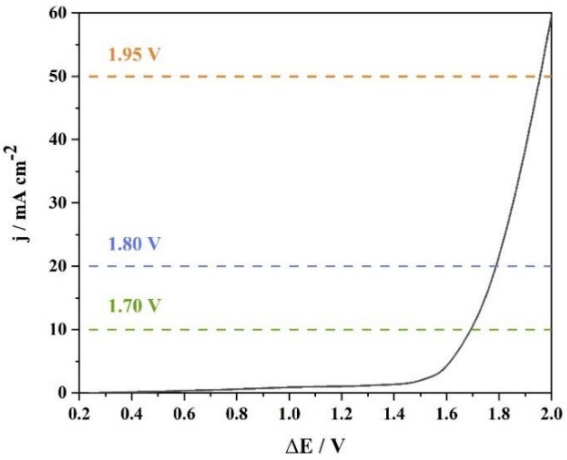


**Figure 22 - Polarization curve in a two-electrode system with NF as the cathode (working electrode) and SS 316L foam as anode (counter electrode).**

It is possible to compare the results obtained for the overall water electrolysis with NF as cathode and 316L SS as the anode, with the individual performance of the electrodes presented in Figure 23. From the LSV recorded for the overall water slitting, a current density of 10 mA $cm^{-2}$ can be generated with a cell potential of 1.70 V. This value is really close to the potential difference of 1.68 V, obtained from the individual voltammograms for the foams. To generate a current density of 20 mA $cm^{-2}$, the actual cell potential was 1.80 V, which was an even better result when compared to the potential difference of 1.91 V calculated through the individual polarization curves.

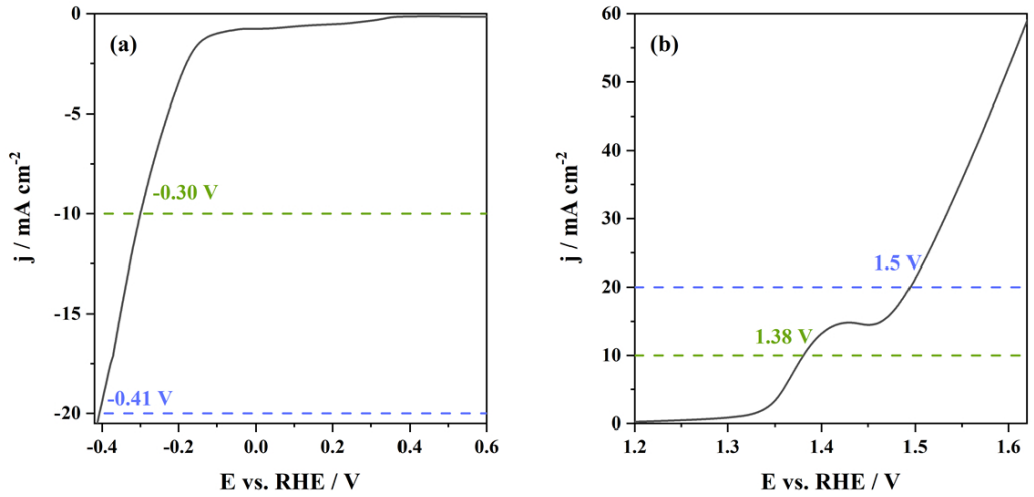


**Figure 23 - Polarization curves recorded at 25 ºC for (a) NF, at 1 mV $s^{-1}$ and (b) SSF, at 2 mV $s^{-1}$.**

From the curve it is possible to observe that to generate a current density of 50 mA $cm^{-2}$, it is applied a potential of 1.95 V. Comparing this value with the ones mentioned in the previous study, 2.4 – 2.5 V, the present result is even better, with the need of lower potential to obtain the same current density.

Hu et al. [37] recorded the polarization curve for the overall water splitting, with NF as cathode and SSM as the anode, in a 1 M KOH solution as the electrolyte, represented in Figure 24. The potentials obtained by these authors for 10, 20, and 50 mA $cm^{-2}$ are very similar to the ones of the present study, proving one more time that the combination of the NF as the cathode and SSF as the anode is suitable to be used in an AWE system.

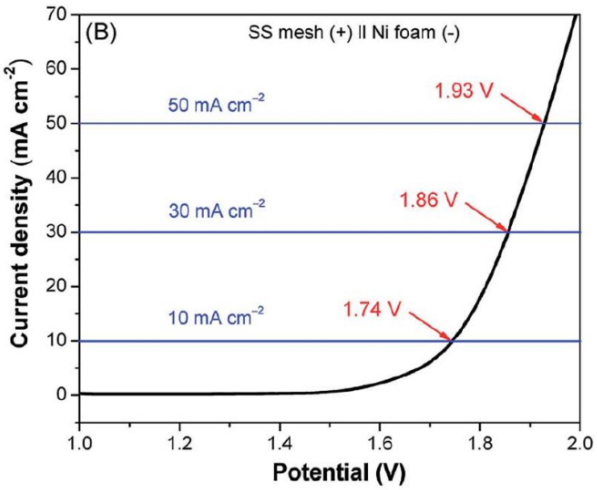


**Figure 24 – Polarization curve in a two-electrode system with NF as the cathode and SSM as the anode. Adapted from [37].**

Based on these results, it is possible to confirm the steady-state performance of the HER, OER and overall water splitting process.

# 4 ELECTROLYZER

## 4.1 METHODOLOGY

### 4.1.1 SYSTEM DESCRIPTION

TecnoVeritas is currently working on a high-efficiency AWE electrolyzer, with the capacity to generate power up to 0.5 MW. This electrolyzer is expected to be a pioneer in Portugal. The structure of the system built by TecnoVeritas is represented in Figure 25. The complete electrolysis system consists of nine main functional blocks: (i) water treatment, (ii) electrolyte preparation, (iii) electrolyzer, (iv) electrolyte temperature control, (v) $O_2$ separation and drying, and (vi) $H_2$ separation and drying, (vii) $O_2$ storage, (viii) $H_2$ storage and (ix) power supply – Figure 26.

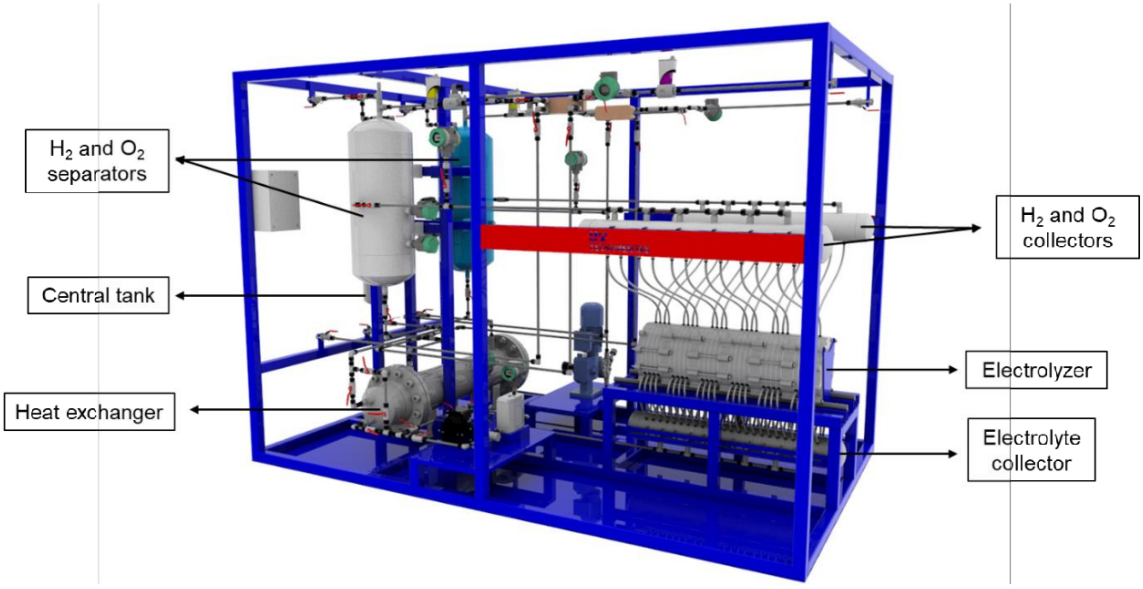


**Figure 25 – Electrolyzer system built by TecnoVeritas.**

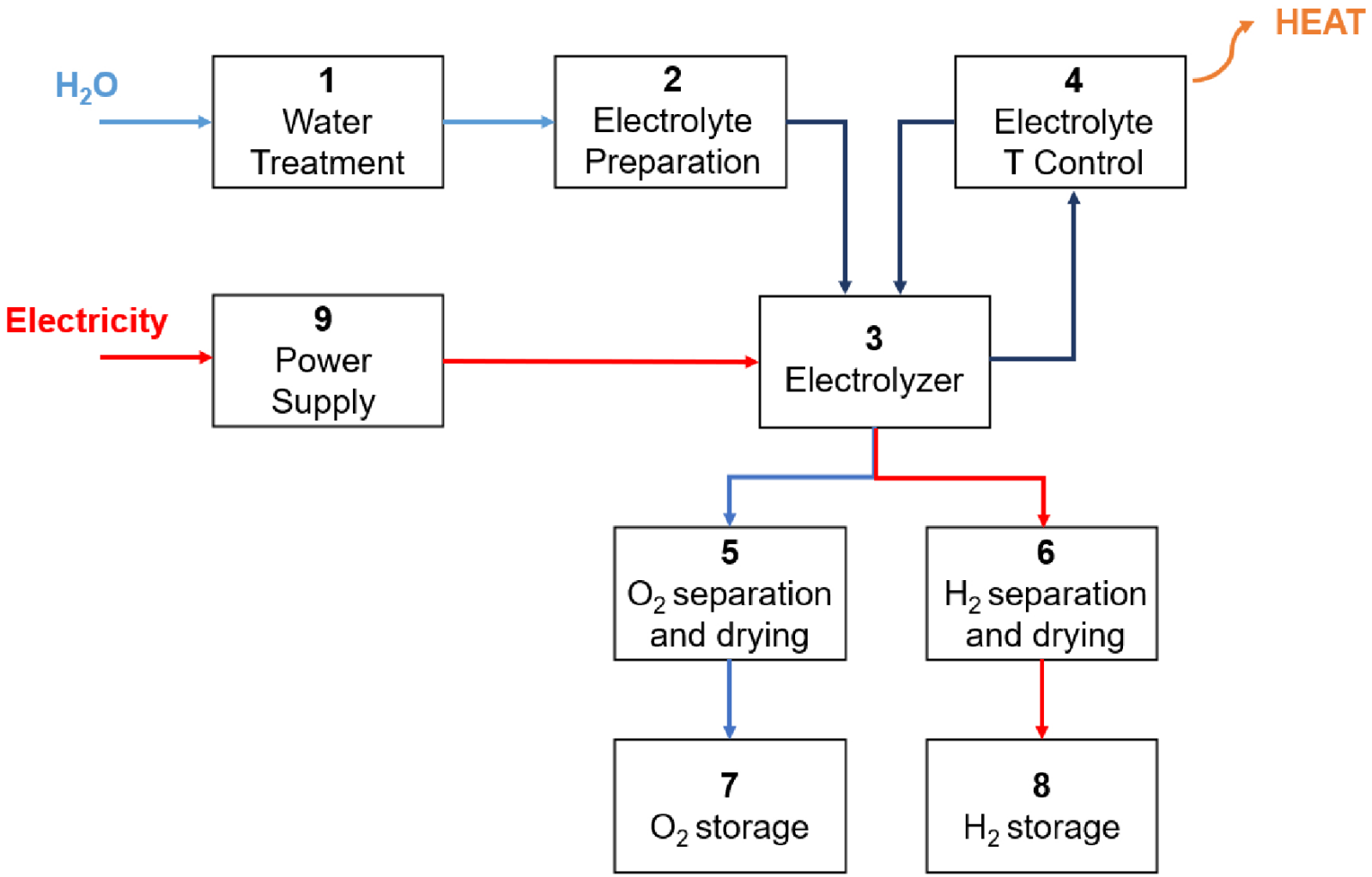


**Figure 26 – Block diagram of the complete electrolyzer.**

The first part of the process consists of obtaining polished water from the network to be used in the electrolyzer without compromising its reliability, namely the diaphragms used. Then, follows the preparation and conditioning of the electrolyte to the operating conditions: a KOH solution with concentration between 30 – 40 wt.%, at 30 bar.

In the third block, before the electrolyte is fed to the electrolyzer, enters the collector. The collector is responsible for directing the electrolyte to the cells simultaneously to prevent the membranes from vibrating and being damaged. During the electrolysis, the gas-liquid mixtures of $H_2$ and $O_2$ leave the cell at the top, to the $H_2$ and $O_2$ collectors.

Right now, the electrolyzer is assembled as represented in Figure 27. It is composed of two electrolysis cells with a zero-gap configuration placed in parallel. Nevertheless, the system is also capable to be adapted to work in series. The external structure of the electrolyzer is composed of two top plates and two rings made of 316L SS. Circular Teflon plates are used close to the external structure as electrical insulators. Close to the Teflon plates, there are used structural rings to support the cell components.

NF and SSF from Nanoshell are used as cathode and anode, respectively. The disk shape electrodes have 3 mm of thickness and 200 mm of diameter. The diaphragm used is the commercially available Agfa Zirfon™ Perl UTO 500, with 200 mm and 500 ± 50 µm of diameter and thickness, respectively.

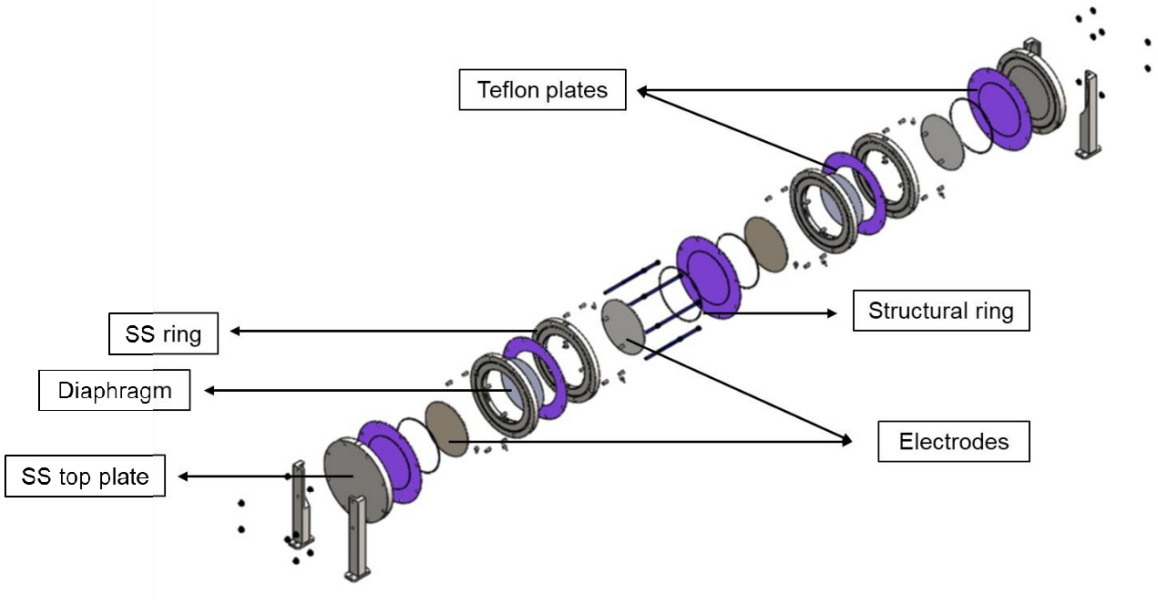


**Figure 27 – Scheme of the electrolyzer.**

A DC power supply provides the electrolysis energy with an output potential range of 0 – 120 V and current up to 100 A.

As the electrolyzer does not have an efficiency of 100 %, the released energy will be used to heat the electrolyte. The temperature of the electrolyte influences its conductivity. Thus, it is important to control the temperature at the entrance of the electrolyzer, to keep it adequate to the concentration, to maximize the efficiency of the electrolysis. So, in the fourth block, a heat exchanger is responsible for cooling the

electrolyte, with cooling water, when the temperature is higher than the desired, before it enters the electrolyzer.

After leaving the electrolyzer, the gases bring some drag solution, so they are dried before being stored. The drying step can be more or less extensive, depending on the percentage of water entrained and on the efficiency of the liquid-gas separators. Depending on the hydrogen's desired final moisture, the drying process can be carried out in several stages. In the end the gases are stored in compressed vessels.

### 4.1.2 THEORETICAL BEHAVIOR OF THE ELECTROLYZER

The theoretical behavior of the electrolyzer developed by TecnoVeritas was simulated, in MATLAB/Simulink, for different temperatures. To do that, the expressions that relate the cell potential and the hydrogen flow produced with the applied current were obtained. All the implementations done in the program are presented in Appendix A.3.

#### 4.1.2.1 Polarization curve

The performance of an electrolyzer is typically studied by plotting its cell potential against the current density, which results in its polarization curve.

As already discussed in section 2.2.1, related to the AWE's thermodynamic considerations, there are several additional parameters that, besides the reversible cell potential, must be considered to the total cell potential. They are the activation overpotentials of the anode and cathode, the ohmic losses of the cell, and the concentration overpotential. Figure 28 shows a typical polarization curve of an AWE electrolyzer and how the mentioned parameters contribute to the cell potential.

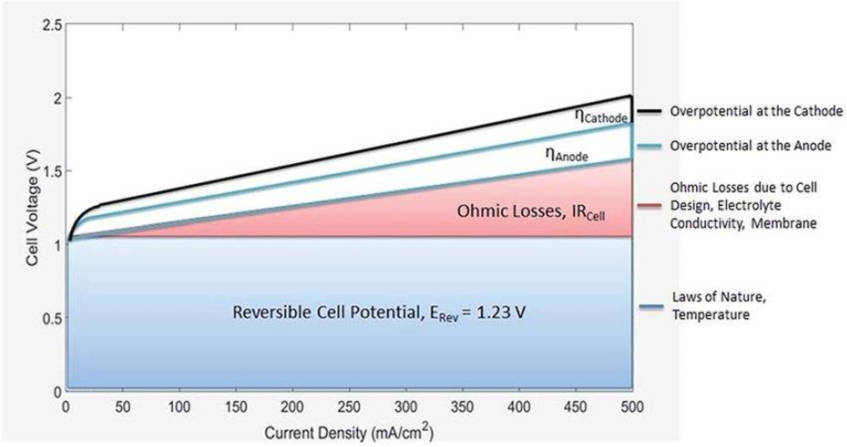


**Figure 28 – Schematic representation of a typically AW electrolyzer's polarization curve and the individual contributions to the cell voltage.**

To predict the theoretical behavior of the electrolyzer developed by TecnoVeritas, the polarization curves at different temperatures were obtained from estimates of the different parameters that contribute to the potential. To start and to simplify the calculations, the reversible cell potential of the electrolyzer was considered constant at all temperatures. The concentration overpotential was neglected, as in the AWE case, its contribution is much lower than the activation overpotentials and ohmic losses.

To calculate the ohmic overpotential, Equation (15) was used. Nevertheless, it was first necessary to estimate the value of the cell's total resistance, which is composed of the resistances counted in Equation (14). Since the $R_{anode}$ and $R_{cathode}$ are generally much lower in comparison to the rest, they have not been calculated. Therefore, the cell's total resistance was considered the sum of the remaining resistances – Equation (39). The contribution of these resistances to the cell voltage of a typical AW electrolyzer is represented in Figure 29.

$$R_{cell} = R_{electrolyte} + R_{membrane} + R_{bubbles} + R_{circuit} \tag{39}$$

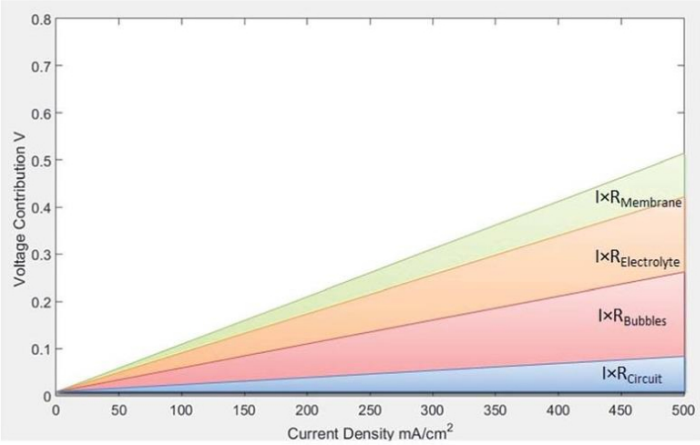


**Figure 29 - Contribution to the cell voltage of the different resistances of a cell.**

The $R_{electrolyte}$ ($\Omega$ cm$^2$) can be expressed by Equation 40, where $\rho_{electrolyte}$ is the specific electrical resistance of the cell ($\Omega$ cm) and $l_{electrolyte}$ is the thickness of the electrolyte i.e. the distance between the electrodes, 0.05 cm). The specific electrical resistance is the inverse of the electrolyte's specific conductivity (S cm$^{-1}$) – Equation 41.

$$R_{electrolyte} = \rho_{electrolyte} \times l_{electrolyte} \tag{40}$$

$$\rho_{electrolyte} = \frac{1}{\sigma_{electrolyte}} \tag{41}$$

The specific conductivity values of a 30 wt.% KOH solution, at different temperatures, used can be consulted in Table 13, Appendix A.2.1. A 1-dimensional lookup table was implemented with this data in the program

Concerning the $R_{membrane}$ ($\Omega$ cm$^2$), another 1-d lookup table was implemented with the data from Table 12, Appendix A.1.

For the $R_{bubbles}$ and $R_{circuit}$ it was not possible to obtain a value or expression for the electrolyzer to be studied. So, their values were estimated, based on Figure 32, It was considered that the portion corresponding to the $R_{bubbles}$ is equal to $R_{electrolyte}$ and the $R_{circuit}$ is equal to the $R_{membrane}$.

The value of the total resistance of the cell was, in the end, divided by the cross-sectional area, $A$.

As can be noticed in Figure 28, the logarithmic shape of the polarization curve is given by the contribution of the activation overpotentials. The activation overpotential for the electrolyzer in this study was estimated based on the polarization curves recorded for the NF and SS foam presented in sections 3.2.2.1 and 3.2.2.2 respectively. The $\eta_{HER}$ and $\eta_{OER}$ were calculated by subtracting to the recorded potential, the contribution of the cell resistance and the equilibrium potential. The cell resistance was calculated following Equation (39). The $R_{membrane}$ was neglected since it was not used in the tests. The $R_{electrolyte}$ was obtained following Equations (40) and (41), where $l_{electrolyte}$ measured was 1 cm$^2$. The specific conductivity values of a 30 wt.% NaOH solution, at different temperatures, are presented in Table 14, Appendix A.2.2. The value of $R_{bubbles}$ was assumed equal to the $R_{electrolyte}$ and $R_{circuit}$ was considered half of $R_{electrolyte}$.

The $\eta_{HER}$ and $\eta_{OER}$ were plotted against the current (A), and trend lines were applied to the data, Figures 30 and 31. The logarithmic expressions, in the form of Equation 43, were obtained for each temperature. The data of the constants are resumed in Tables 10 and 11. For the OER, the overpotential at 25 ºC was neglected, as it did not follow the trend of the remaining temperatures.

$$\eta/V = C_1 \ln(I/A) + C_2 \tag{42}$$

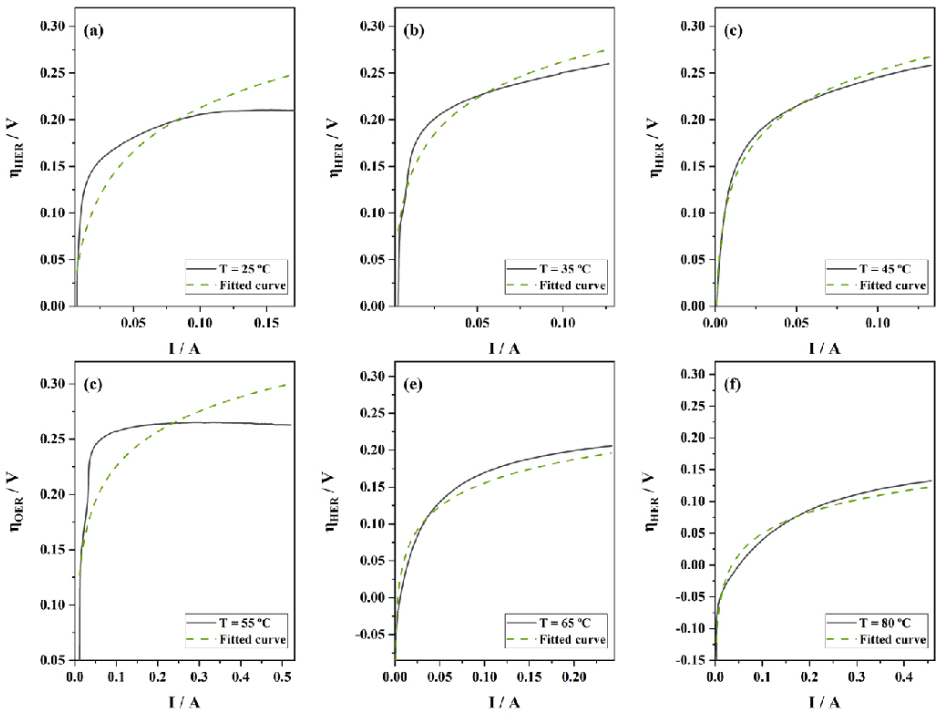


**Figure 30 – HER overpotential as function of the current at different temperatures: (a) 25 ºC, (b) 35 ºC, (c), 45 ºC, (d) 55 ºC, (e) 65 ºC and (f) 80 ºC.**

**Table 10 – Constants obtained for the logarithmic trend lines, at different temperatures, for the $\eta_{HER}$ vs. I.**

| | 25 ºC | 35 ºC | 45 ºC | 55 ºC | 65 ºC | 80 ºC |
|---|---|---|---|---|---|---|
| $C_1$ | 0.068 | 0.056 | 0.055 | 0.056 | 0.046 | 0.048 |
| $C_2$ | 0.368 | 0.391 | 0.378 | 0.329 | 0.261 | 0.161 |

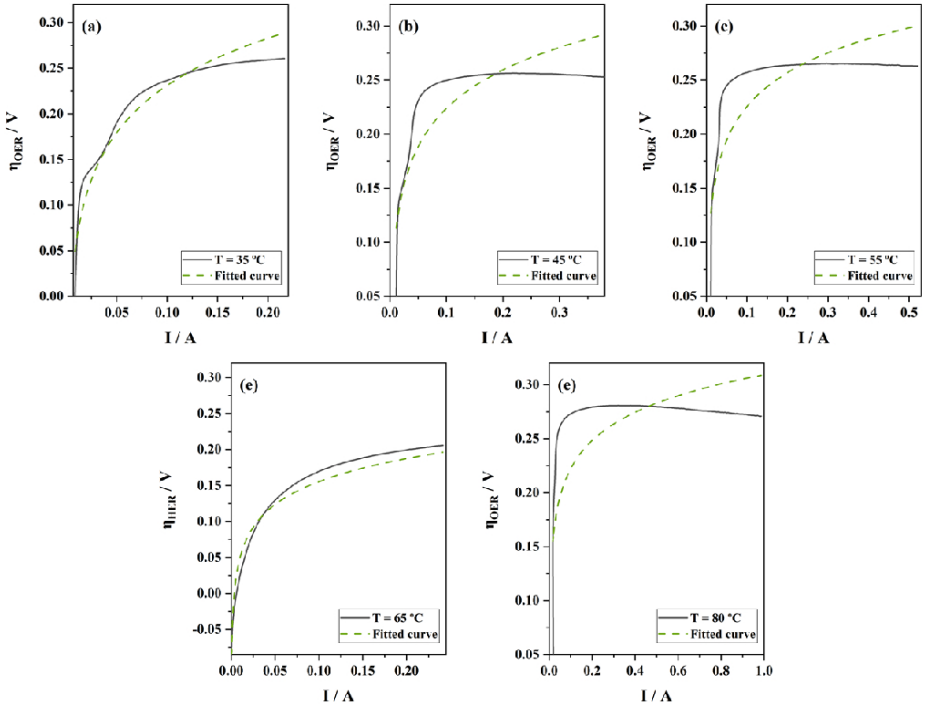


**Figure 31 – OER overpotential as function of the current, at different temperatures: (a) 35 ºC, (b) 45 ºC, (c) 55 ºC, (d) 65 ºC and (e) 80 ºC.**

**Table 11 - Constants obtained for the logarithmic trend lines, at different temperatures, for the $\eta_{OER}$ vs. I.**

| | 35 ºC | 45 ºC | 55 ºC | 65 ºC | 80 ºC |
|---|---|---|---|---|---|
| $C_1$ | 0.075 | 0.051 | 0.045 | 0.043 | 0.038 |
| $C_2$ | 0.403 | 0.342 | 0.330 | 0.327 | 0.309 |

The expressions were used to estimate the activation overpotentials, Figure 32, and the data was resumed in 2-dimensional lookup tables in the Matlab/Simulink.

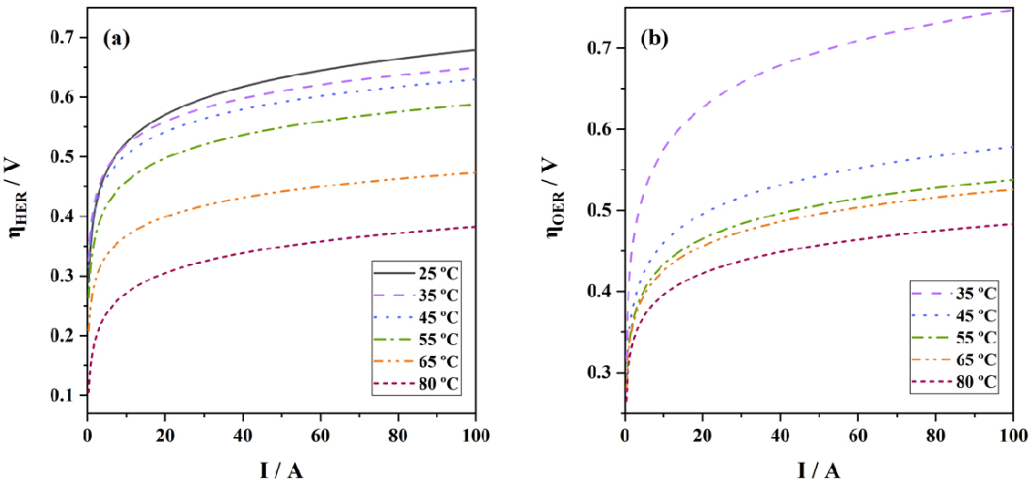


**Figure 32 – Contributions of the activation overpotential of (a) cathode and (b) anode, for the total cell potential, at different temperatures.**

It is crucial to keep in mind that the data used to estimate the activation overpotentials was recorded in a different electrolyte than the one that will be used in the electrolyzer. As already seen in the state-of-the-art section, both solutions' conductivity varies, as well as the overpotentials. However, it was decided to proceed with the calculations anyway, because it was considered that the difference would not have a significant impact on the total potential of the cell, which could jeopardize the veracity of the results.

### 4.1.2.2 Gas production

In general, the flow rate of a gaseous product can be calculated theoretically considering the Faraday law of electrolysis – Equation (43).

$$n = \frac{It}{Fz} \tag{43}$$

where $n$ is the number of moles, $I$ is the current in amperes, $t$ is the time in seconds and $z$ is the proportionality constant called electrochemical equivalent. In the present case, for each $H_2O$ molecule consumed to form $H_2$, there is a transfer of 2 electrons, as can be seen in Equation (2), so the constant $z$ will be equal to 2.

Dividing both members of the equation by time and considering the molecular weight of the hydrogen, $MW_{H_2}$ (kg mol$^{-1}$), the mass flow, $Q_{H_2}$ ( kg s$^{-1}$), is obtained – Equation (44).

$$Q_{H_2} = \frac{I}{2F} \times MW_{H_2} \tag{44}$$

Using the ideal gas law, $PV = nRT$, it is possible to calculate the production of hydrogen in volume, $V_{H_2}$ (L s$^{-1}$), from Equation (45).

$$V_{H_2} = \frac{n_{H2}RT}{P} \tag{45}$$

Typically, the efficiency of an alkaline water electrolyzer ranges from 62 to 82 %, as shown in Table 2. Considering the average value of 70 %, it is possible to obtain, more precisely, the theoretical value of the hydrogen production.

### 4.1.3 TIGHTNESS TESTS

The tightness tests were carried out by introducing water into the closed electrolyzer, without cell components (membranes and electrodes), as shown in Figure 33a. Once the system was filled with water, the pressure was gradually increased to the desired level, around 40 bar. The pressure was measured with the manometer in Figure 33b. The tests were repeated several times, with a duration of 30 minutes to 1 hour.

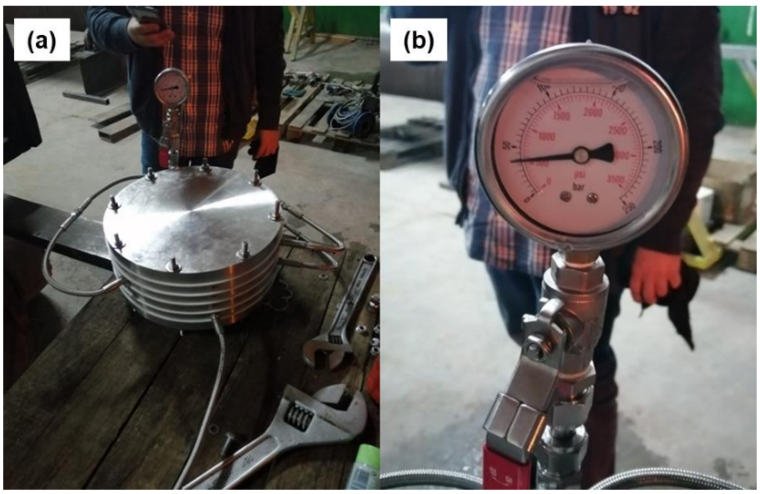


**Figure 33 – (a) Assembly of the electrolyzer for the tightness tests and (b) pressure read on the manometer.**

## 4.2 RESULTS AND DISCUSSION

### 4.2.1 THEORETICAL BEHAVIOR OF THE ELECTROLYZER

The polarization curves obtained from the model developed in MATLAB/Simulink are present in Figure 34. Since the electrolyzer being developed in TecnoVeritas consists in two electrolysis cells, the overall potential is double that obtained for one cell.

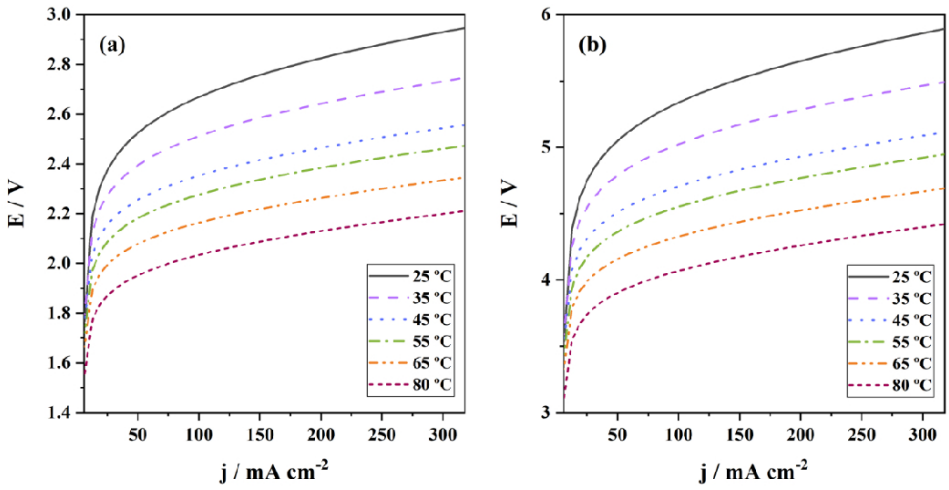


**Figure 34 – Polarization curves obtained from the theoretical model developed in MATLAB/Simulink, at different temperatures, (a) for a single electrolysis cell and (b) for the electrolyzer developed by TecnoVeritas, which has 2 electrolysis cells.**

For now, it is planned that the electrolyzer being developed in TecnoVeritas will be working at room temperature, around 25 ºC. By observing the figure, it is possible to estimate that the potential, at that temperature, necessary to generate 300 mA $cm^{-2}$, a typical current density applied in the AWE system, is around 5.85 V (2.93 V in each electrolysis cell). The potential recorded for one cell is a bit high compared to the typical value found in the literature, for high-efficient alkaline water electrolyzers, which is around 2.2 V. Nevertheless, as expected, the potential decreases with the temperature rise. So, if TecnoVeritas desire to increase the efficiency of the electrolyzer, it can optimize the system to work at higher temperatures. At 80 ºC, the potential necessary to generate 300 mA $cm^{-2}$ is 2.2 V, the same as the one pointed in the literature.

With respect to the theoretical production of hydrogen, working at 300 mA $cm^{-2}$, 25 ºC and 30 bar, it is expected a production, in terms of mass of 2.48 g $h^{-1}$, and in terms of volume of 1.02 L $h^{-1}$ per electrolysis cell. This means that the theoretical hydrogen production in the current electrolysis system is close to 5 g $h^{-1}$ in terms of mass and 2.04 L $h^{-1}$ in terms of volume. In the optimized system, at 80 ºC, the production in terms of volume increases to 1.2 L $h^{-1}$ per electrolysis cell, and 2.4 L $h^{-1}$ in the projected electrolyzer.

### 4.2.2 TIGHTNESS TESTS

During the tightness tests, it is important to pay attention to water leaks on the system and the sound of air escaping, before increasing the pressure of the system, because these phenomena are a sign that the system is not fully closed without air. So, when the developed electrolyzer was subjected to these tests, the pressure was only increased after verifying if the system passed successfully in this first part. If not, the system was adjusted to be properly closed until no more leaks were observed.

When proceeding to the gradual increase in pressure, it was checked if there was no pressure drop during the established time. Practically all test repetitions did not show a pressure drop. In the exceptional cases where a slight pressure drop was observed, the electrolyzer was checked again for the problem to be identified and resolved. Thus, it was concluded that the system passed the tightness test and was able to proceed to the remaining tests.

# 5 CONCLUSION

The way forward for future energy systems is through hydrogen and water electrolysis is seen as the greatest method for its production. Therefore, making water electrolysis technologies efficient and market-competitive is fundamental to a hydrogen economy to thrive, and achieve the goal of decarbonization by 2050.

TecnoVeritas is currently developing a high-efficient alkaline water electrolyzer, which is expected to be pioneer in Portugal. Currently the electrolyzer is composed of two electrolysis cells, nevertheless, the system is built in order to be able to incorporate a greater number of cells and achieve higher hydrogen production. There is also the possibility to scale-up the current system.

In the present work, the complete system was described. The electrolyzer incorporates several features that contribute to increasing efficiency, making it a very innovative technology when compared to the current electrolyzers available commercially. It is fundamental to emphasize (i) the high working pressure of 30 bar, which drastically reduces the energy required to compress the gases to storage pressure, (ii) the high turbulence generated in the cells, which facilitates the detachment of the gas bubbles of the electrodes, allowing greater availability of the electrodes for electrolysis, (iii) the use of a high-performance diaphragm, (iv) the zero-gap configuration, that minimize the inter-electrode distance, and therefore the electrolyte resistance, (v) the use of porous electrodes, with high catalytic effect and (v) an electrical supply without harmonic distortion.

A project of this dimension requires extensive research and consists of a series of steps necessary to ensure a good operation. The work brought forward in this thesis covered a considerable amount of these steps.

In order to build an efficient electrolyzer, several operational parameters need to be optimized. The choice of the electrode materials is by far one of the main factors influencing the efficiency of the reactions. From the state-of-the-art, it was concluded that porous electrodes present higher catalytic behavior because of their higher active surface area. Ni and SS are two inexpensive materials indicated as good electrocatalysts towards the HER and OER, respectively. So, NF and SS foam were chosen as cathode and anode, respectively, for the electrolyzer being developed by TecnoVeritas. To validate this choice, their electrocatalytic behavior was studied using CV, LSV and CP.

The complete CVs were obtained to study the redox behavior of the foams at 25 and 80 ºC. For both foams, the current densities reached at 80 ºC were higher, and the potentials where the processes occur were lower. These results can translate into the idea that temperature favors the redox processes, and therefore the HER and OER. The results were compared to Ni and SS bulk electrodes found in the literature. All the processes found in the literature were also identified . The current densities reached were higher, which was expected because foam electrodes have higher catalytic activity. CV was also used to record the CVs on the double layer region to access the ECSA. The NF presents an ECSA of 820 $cm^2$, with a roughness factor of 82 and the SSF presents an ECSA of 179 $cm^2$ and a roughness factor of 39.

The LSV tests done in the temperature range of 25 – 80 ªC, for the NF and SSF agreed with the first conclusion drawn from the complete CVs, that the catalytic activity of the foams is proportional to the temperature rise.

Besides the catalytic activity of the electrode, the stability was also evaluated by CP. At 50 mA $cm^{-2}$ the electrodes have shown themselves stable for the 16 h test. The NF potential varied about 0.02 V stabilizing at around -0.7 V, while the potential of the SS foam stabilized at 1.8 V, suffering a variation of 1 V during the test. From this result it was possible to predict that the potential necessary to generate 50 mA $cm^{-2}$ is 2.4 – 2.5 V.

Furthermore, since the foams showed a good individual performance, it was also evaluated its behavior towards the overall water electrolysis. From the polarization curve obtained, it was concluded that the potential necessary to generate 10, 20 and 50 mA $cm^{-2}$ is 1.70 V, 1.80 V e 1.95 V, respectively. The potential at 10 and 20 mA $cm^{-2}$ is in accordance with the potential difference calculated from the individual LSVs of the foams. And at 50 mA $cm^{-2}$, the result was even better than expected based on the stability tests. Based on these results, it is possible to confirm the steady-state performance of the HER, OER, and overall water splitting process.

Overall, it can be said that the electrodes behaved as expected. The NF and SS foam showed great catalytic behavior towards HER and OER, respectively, at all temperatures, but especially at higher ones. They also presented themselves as stable at the conditions to which they were subjected. So, it was possible to validate their choice as cathode and anode for the electrolyzer.

Using the results obtained from the study of the foams, the behavior of the electrolyzer was simulated, at different temperatures, resorting MATLAB/Simulink. From the polarization curves, it was possible to estimate that, to the electrolyzer generates a current density of 300 mA $cm^{-2}$, it is necessary to apply 5.85 V, at 25 ºC and the hydrogen production capacity in terms of volume is 2.04 L $h^{-1}$. If the system was optimized to work at 80 ºC, the potential would decrease to 4.4 V and the hydrogen production would increase to 2.4 L $h^{-1}$.

Lastly, before proceeding to assemble the electrolyzer cells and perform tests on the electrolyzer, tightness tests were carried out to verify if the external structure of the electrolyzer yielded to such high pressures. In the vast majority of the test repetitions, there was no leakage or pressure drop. Thus, it was concluded that the system passed the tightness test and was able to proceed to the remaining tests.

# 6 FUTURE WORK

The high-efficiency electrolyzer proposed by TecnoVeritas is very close to being complete. Unfortunately, during the present work, it was not possible to finish its construction in order to test it and compare with the predicted theoretical behavior.

When the electrolyzer is finished, several tests will be done in order to find the most optimized form of the electrolyzer. It is then part of the plan, to study the hydrogen production of the electrolyzer varying several parameters: (i) the pressure of the system between 30 and 40 bar, (ii) the electrolyte concentration between 30 and 40 wt.% of KOH, and (iii) the configuration of the cells, placed in series or in parallel. Besides, based on the work presented in this thesis, it is suggested to optimize the system in order to work at higher temperatures, for example at 80 ºC, rather than at room temperature, and test it.

Also, it will be advantageous for the efficiency of the electrolyzer to test new electrocatalysts. The materials presented in the state-of-the-art are seen as the most widely used at an industrial level, because they are cheap materials with good catalytic properties. Nevertheless, this is a trendy topic that is being the subject of a lot of research, and new materials are suggested in the literature with a performance quite above that of Ni and SS, within reasonable prices. Ni alloys, such as Raney Ni and NiMo for the HER; NiFe oxides and (oxy)hydroxides and Inconel for OER.

Once the system is optimized, production capacity can be increased by increasing the number of cells in the system, increasing the cross-sectional area, by increasing the area of the electrodes, and/or doing a scale-up of the current system. As mentioned, the expected maximum capacity of the system is 0.5 MW. To reach such power, working at 300 mA $cm^{-2}$ and 80 ºC, the system will require 96 electrolysis cells with electrodes' diameter of 1 m. In this case, the maximum hydrogen production will be around 0.72 $m^3$ $day^{-1}$ per cell, which gives a total production of 69 $m^3$ $day^{-1}$.

Finally, although hydrogen storage is not the central topic of this work, it should be noted that it is a fundamental point for the hydrogen production to be as efficient as possible. It is planned that the hydrogen produced will be stored as compressed gas. This is the most well-established method of hydrogen storage. Nevertheless, there are already quite interesting and promising alternative technologies present in the literature. Chemical-based hydrogen storage is been seen as the best long-term solution to address the safety issues that the traditional systems present, as well as the solution to store hydrogen in a smaller volume. This hydrogen storage method still has a long way to go, but it is worth giving an opportunity and invest in more thorough research on the subject.

## REFERENCES


[1] BP, Full report – BP Statistical Review of World Energy 2019, (n.d).

[2] EIA - Today in Energy, (n.d.). https://www.eia.gov/todayinenergy/detail.php?id=41433 (accessed April 19, 2020).

[3] International Energy Agency, World energy balances: An Overview, J. Chem. Inf. Model. 53 (2019) 1689–1699. https://doi.org/10.1017/CBO9781107415324.004

[4] Greenhouse gas concentrations in atmosphere reach yet another high | World Meteorological Organization, (n.d.). https://public.wmo.int/en/media/press-release/greenhouse-gas-concentrations-atmosphere-reach-yet-another-high (accessed April 19, 2020).

[5] Global Climate Report - Annual 2019 | State of the Climate | National Centers for Environmental Information (NCEI), (n.d.). https://www.ncdc.noaa.gov/sotc/global/201913 (accessed April 19, 2020).

[6] What is the Paris Agreement? | UNFCCC, (n.d.). https://unfccc.int/process-and-meetings/the-paris-agreement/what-is-the-paris-agreement (accessed October 2, 2020).

[7] Communication COM/2020/301: A hydrogen strategy for a climate-neutral Europe | Knowledge for policy, (n.d.). https://knowledge4policy.ec.europa.eu/publication/communication-com2020301-hydrogen-strategy-climate-neutral-europe_en (accessed December 27, 2020).

[8] T. da Silva Veras, T.S. Mozer, D. da Costa Rubim Messeder dos Santos, A. da Silva César, Hydrogen: Trends, production and characterization of the main process worldwide, Int. J. Hydrogen Energy 42 (2017) 2018–2033. https://doi.org/10.1016/j.ijhydene.2016.08.219

[9] IRENA, Hydrogen From Renewable Power: Technology outlook for the energy transition, 2018. www.irena.org.

[10] S. Rebouillat, M. Lyons, M. Brandon, and R. Doyle, Paving the Way to The Integration of Smart Nanostructures : Part II : Nanostructured Microdispersed Hydrated Metal Oxides for Electrochemical Energy Conversion and Storage Applications. Int. J. of Electrochemical Science, 6 (2011) 5830–5917.

[11] FCHJU. (2016). CertifHy – Developing a European Framework for the generation of guarantees of origin for green hydrogen: Definition of Green Hydrogen [6]. https://ec.europa.eu/jrc/sites/jrcsh/files/Vanhoudt%20Definition%20of%20Green%20Hydrogen%20SFEM.pdf

[12] Hydrogen – Tracking Energy Integration – Analysis - IEA, (n.d.). https://www.iea.org/reports/tracking-energy-integration/hydrogen (accessed April 19, 2020).

[13] M. David, C. Ocampo-Martínez, R. Sánchez-Peña, Advances in alkaline water electrolyzers: A

review, J. Energy Storage 23 (2019) 392–403. https://doi.org/10.1016/j.est.2019.03.001

[14] P. Nikolaidis, A. Poullikkas, A comparative overview of hydrogen production processes, Renew. Sustain. Energy Rev. 67 (2017) 597–611. https://doi.org/10.1016/j.rser.2016.09.044

[15] T. N. Veziroğlu, S. Şahi˙n, 21st Century's energy: hydrogen energy system, Energy Conv. Manag. 49 (2008) 1820–1831. https://doi.org/10.1016/j.enconman.2007.08.015

[16] C.M. Kalamaras, A.M. Efstathiou, Hydrogen Production Technologies: Current State and Future Developments, Conf. Pap. Energy 2013 (2013) 1–9. https://doi.org/10.1155/2013/690627

[17] D.M.F. Santos, C.A.C. Sequeira, J.L. Figueiredo, Hydrogen Production by Alkaline Water Electrolysis, Quim. Nova 36 (2013) 1176–1193. http://dx.doi.org/10.1590/S0100-40422013000800017

[18] M.M. Rashid, M.K. Al Mesfer, H. Naseem, M. Danish, Hydrogen Production by Water Electrolysis: A Review of Alkaline Water Electrolysis, PEM Water Electrolysis and High Temperature Water Electrolysis, Int. J. Eng. Adv. Technol. (2015) 2249–8958. https://citeseerx.ist.psu.edu/viewdoc/download?doi=10.1.1.673.5912&rep=rep1&type=pdf

[19] O. Schmidt, A. Gambhir, I. Staffell, A. Hawkes, J. Nelson, S. Few, Future cost and performance of water electrolysis: An expert elicitation study, Int. J. Hydrogen Energy 42 (2017) 30470–30492. https://doi.org/10.1016/j.ijhydene.2017.10.045

[20] C.K. Kjartansdóttir, P. Moller, Development of Hydrogen Electrodes for Alkaline Water Electrolysis, DTU Mech. Eng. (2014) 189. https://doi.org/http://dx.doi.org/10.1016/j.ijhydene.2013.04.101

[21] Q. Feng, X.Z. Yuan, G. Liu, B. Wei, Z. Zhang, H. Li, H. Wang, A review of proton exchange membrane water electrolysis on degradation mechanisms and mitigation strategies, J. Power Sources 366 (2017) 33–55. https://doi.org/10.1016/j.jpowsour.2017.09.006

[22] M. Schalenbach, G. Tjarks, M. Carmo, W. Lueke, M. Mueller, D. Stolten, Acidic or Alkaline? Towards a New Perspective on the Efficiency of Water Electrolysis, J. Electrochem. Soc. 163 (2016) F3197–F3208. https://doi.org/10.1149/2.0271611jes

[23] M. Felgenhauer, T. Hamacher, State-of-the-art of commercial electrolyzers and on-site hydrogen generation for logistic vehicles in South Carolina, Int. J. Hydrogen Energy 40 (2015) 2084–2090. https://doi.org/10.1016/j.ijhydene.2014.12.043

[24] K. Zeng, D. Zhang, Recent progress in alkaline water electrolysis for hydrogen production and applications, Prog. Energy Combust. Sci. 36 (2010) 307–326. https://doi.org/10.1016/j.pecs.2009.11.002

[25] W. Wang, X. Wei, D. Choi, X. Lu, G. Yang, C. Sun, Electrochemical cells for medium-and large-scale energy storage: Fundamentals, in Advances in Batteries for Medium and Large-Scale Energy Storage. Woodhead Publishing Series in Energy, 2015: pp. 3–28. https://doi.org/10.1016/B978-1-78242-013-2.00001-7

[26] K. Zouhri, S.Y. Lee, Evaluation and optimization of the alkaline water electrolysis ohmic polarization: Exergy study, Int. J. Hydrogen Energy 41 (2016) 7253–7263. https://doi.org/10.1016/j.ijhydene.2016.03.119

[27] M. Carmo, D. Stolten, Energy storage using hydrogen produced from excess renewable electricity: Power to hydrogen, in Science and Engineering of Hydrogen-Based Energy Technologies. Hydrogen Production and Practical Applications in Energy Generation, in Elsevier Generation, Elsevier Inc., 2018: pp. 165–199. https://doi.org/10.1016/B978-0-12-814251-6.00004-6

[28] M. Wang, Z. Wang, X. Gong, Z. Guo, The intensification technologies to water electrolysis for hydrogen production - A review, Renew. Sustain. Energy Rev. 29 (2014) 573–588. https://doi.org/10.1016/j.rser.2013.08.090

[29] Fundamentos teóricos de eletrocoagulação, (2014) 25–55.

[30] V.D. Jović, B.M. Jović, U. Lačnjevac, N. V. Krstajić, P. Zabinski, N.R. Elezović, Accelerated service life test of electrodeposited NiSn alloys as bifunctional catalysts for alkaline water electrolysis under industrial operating conditions, J. Electroanal. Chem. 819 (2018) 16–25. https://doi.org/10.1016/j.jelechem.2017.06.011

[31] C.F. Zinola, M.E. Martins, E.P. Tejera, N.P. Neves, Electrocatalysis: Fundamentals and Applications, Int. J. Electrochem. 2012 (2012) 1–2. https://doi.org/10.1155/2012/874687

[32] D. Pletcher, X. Li, Prospects for alkaline zero gap water electrolysers for hydrogen production, Int. J. Hydrogen Energy 36 (2011) 15089–15104. https://doi.org/10.1016/j.ijhydene.2011.08.080

[33] M. Wang, Z. Wang, X. Gong, Z. Guo, The intensification technologies to water electrolysis for hydrogen production - A review, Renew. Sustain. Energy Rev. 29 (2014) 573–588. https://doi.org/10.1016/j.rser.2013.08.090

[34] M. Tahir, L. Pan, F. Idrees, X. Zhang, L. Wang, J.J. Zou, Z.L. Wang, Electrocatalytic oxygen evolution reaction for energy conversion and storage: A comprehensive review, Nano Energy 37 (2017) 136–157. https://doi.org/10.1016/j.nanoen.2017.05.022

[35] M. Gong, D.Y. Wang, C.C. Chen, B.J. Hwang, H. Dai, A mini review on nickel-based electrocatalysts for alkaline hydrogen evolution reaction, Nano Res. 9 (2016) 28–46. https://doi.org/10.1007/s12274-015-0965-x

[36] A.N. Colli, H.H. Girault, A. Battistel, Non-precious electrodes for practical alkaline water electrolysis, Materials (Basel). 12 (2019) 1–17. https://doi.org/10.3390/ma12081336

[37] X. Hu, X. Tian, Y.W. Lin, Z. Wang, Nickel foam and stainless steel mesh as electrocatalysts for hydrogen evolution reaction, oxygen evolution reaction and overall water splitting in alkaline media, RSC Adv. 9 (2019) 31563–31571. https://doi.org/10.1039/c9ra07258f

[38] K.I. Siwek, S. Eugénio, D.M.F. Santos, M.T. Silva, M.F. Montemor, 3D nickel foams with

controlled morphologies for hydrogen evolution reaction in highly alkaline media, Int. J. Hydrogen Energy 44 (2019) 1701–1709. https://doi.org/10.1016/j.ijhydene.2018.11.070

[39] M.I. Jamesh, Recent progress on earth abundant hydrogen evolution reaction and oxygen evolution reaction bifunctional electrocatalyst for overall water splitting in alkaline media, J. Power Sources 333 (2016) 213–236. https://doi.org/10.1016/j.jpowsour.2016.09.161

[40] G. Ou, P. Fan, H. Zhang, K. Huang, C. Yang, W. Yu, H. Wei, M. Zhong, H. Wu, Y. Li, Large-scale hierarchical oxide nanostructures for high-performance electrocatalytic water splitting, Nano Energy 35 (2017) 207–214. https://doi.org/10.1016/j.nanoen.2017.03.049

[41] Chemistry LibreTexts, 4.6 Pourbaix Diagrams. (2020). https://chem.libretexts.org/Bookshelves/Inorganic_Chemistry/Book%3A_Introduction_to_Inorganic_Chemistry/04%3A_Redox_Stability_and_Redox_Reactions/4.06%3A_Pourbaix_Diagrams (accessed July 10, 2020).

[42] F. Yu, F. Li, L. Sun, Stainless steel as an efficient electrocatalyst for water oxidation in alkaline solution, Int. J. Hydrogen Energy 41 (2016) 5230–5233. https://doi.org/10.1016/j.ijhydene.2016.01.108

[43] G.R. Zhang, L.L. Shen, P. Schmatz, K. Krois, B.J.M. Etzold, Cathodic activated stainless steel mesh as a highly active electrocatalyst for the oxygen evolution reaction with self-healing possibility, J. Energy Chem. 49 (2020) 153–160. https://doi.org/10.1016/j.jechem.2020.01.025

[44] J. Zhang, T. Wang, D. Pohl, B. Rellinghaus, R. Dong, S. Liu, X. Zhuang, X. Feng, Interface Engineering of $MoS_2/Ni_3S_2$ Heterostructures for Highly Enhanced Electrochemical Overall-Water-Splitting Activity , Angew. Chemie. 128 (2016) 6814–6819. https://doi.org/10.1002/ange.201602237

[45] E. Amores, J. Rodríguez, C. Carreras, Influence of operation parameters in the modeling of alkaline water electrolyzers for hydrogen production, Int. J. Hydrogen Energy 39 (2014) 13063–13078. https://doi.org/10.1016/j.ijhydene.2014.07.001

[46] J. Brauns, T. Turek, Alkaline water electrolysis powered by renewable energy: A review, Processes 8 (2020). https://doi.org/10.3390/pr8020248

[47] R.J. Gilliam, J.W. Graydon, D.W. Kirk, S.J. Thorpe, A review of specific conductivities of potassium hydroxide solutions for various concentrations and temperatures, Int. J. Hydrogen Energy 32 (2007) 359–364. https://doi.org/10.1016/j.ijhydene.2006.10.062

[48] F. Allebrod, C. Chatzichristodoulou, P.L. Mollerup, M.B. Mogensen, Electrical conductivity measurements of aqueous and immobilized potassium hydroxide, Int. J. Hydrogen Energy 37 (2012) 16505–16514. https://doi.org/10.1016/j.ijhydene.2012.02.088

[49] N. V. Kuleshov, V.N. Kuleshov, S.A. Dovbysh, E.Y. Udris, S.A. Grigor'ev, Y.A. Slavnov, L.A. Korneeva, Polymeric composite diaphragms for water electrolysis with alkaline electrolyte, Russ.

J. Appl. Chem. 89 (2016) 618–621. https://doi.org/10.1134/S1070427216040157

[50] V.M. Rosa, M.B.F. Santos, E.P.D.A. Silva, New Materials for Water Electrolysis Diaphragms, 20 (1995) 697–700.

[51] R. Coquet, ZIRFON PERL ™ separator for alkaline water electrolysis Agfa-Gevaert Group – Historical highlights, Hann. Messe. (2016) 1–15.

[52] P. Vermeiren, W. Adriansens, J.P. Moreels, R. Leysen, The Composite Zirfon® Separator for Alkaline Water Electrolysis, in: Hydrog. Power Theor. Eng. Solut., Springer Netherlands, 1998: pp. 179–184. https://doi.org/10.1007/978-94-015-9054-9_21

[53] R. Phillips, C.W. Dunnill, Zero gap alkaline electrolysis cell design for renewable energy storage as hydrogen gas, RSC Adv. 6 (2016) 100643–100651. https://doi.org/10.1039/c6ra22242k

[54] A.P. Fickett, F.R. Kalhammer, Water Electrolysis, in: K.E. Cox, K.D. Williamson (Eds.), Hydrogen: Its Technology Implications: Hydrogen Production Technology, Boca Raton, 2017. https://books.google.pt/books?hl=pt-PT&lr=&id=vktnDwAAQBAJ&oi=fnd&pg=PT12&dq=fundamentals+of+water+electrolysis&ots=gqsDeWQHSv&sig=0N-z7hvGhNc78T0ElADZJxTiK90&redir_esc=y#v=onepage&q=fundamentals of water electrolysis&f=false (accessed May, 3).

[55] J.O. Abe, A.P.I. Popoola, E. Ajenifuja, O.M. Popoola, Hydrogen energy, economy and storage: Review and recommendation, Int. J. Hydrogen Energy 44 (2019) 15072–15086. https://doi.org/10.1016/j.ijhydene.2019.04.068

[56] D.P. Broom, C.J. Webb, G.S. Fanourgakis, G.E. Froudakis, P.N. Trikalitis, M. Hirscher, Concepts for improving hydrogen storage in nanoporous materials, Int. J. Hydrogen Energy 44 (2019) 7768–7779. https://doi.org/10.1016/j.ijhydene.2019.01.224

[57] R.A. Varin, T. Czujko, Z.S. Wronski, P. Prachi, M.M. Wagh, G. Aneesh, Chapter 2 “ Heart ” of Solid State Hydrogen Storage, Adv. Energy Power 4 (2009) 11–22. https://doi.org/10.13189/aep.2016.040202

[58] H. Barthelemy, M. Weber, F. Barbier, Hydrogen storage: Recent improvements and industrial perspectives, Int. J. Hydrogen Energy 42 (2017) 7254–7262. https://doi.org/10.1016/j.ijhydene.2016.03.178

[59] O. Pesonen, T. Alakunnas, Energy Storage - A Missing Piece of the Puzzle for the Self-Sufficient Living, 2017. https://www.theseus.fi/bitstream/handle/10024/136086/B 14 2017 Pesonen Alakunnas.pdf?sequence=1&isAllowed=y%0Ahttps://www.lapinamk.fi/loader.aspx?id=3b80e74a-7843-41c8-baad-e5338f5eb4b3

[60] R. Moradi, K.M. Groth, Hydrogen storage and delivery: Review of the state of the art technologies and risk and reliability analysis, Int. J. Hydrogen Energy 44 (2019) 12254–12269.

https://doi.org/10.1016/j.ijhydene.2019.03.041

[61] I. Iordache, D. Schitea, R. Buga, A. Marinoiu, M. Balan, I. Stefanescu, Hydrogen underground storage in Romania, the potential, actors and relevant circumstances, 20th World Hydrog. Energy Conf. WHEC 2014. 2 (2014) 1352–1355.

[62] E. Rivard, M. Trudeau, K. Zaghib, Hydrogen storage for mobility: A review, Materials (Basel). 12 (2019). https://doi.org/10.3390/ma12121973

[63] M. Niermann, A. Beckendorff, M. Kaltschmitt, K. Bonhoff, Liquid Organic Hydrogen Carrier (LOHC) – Assessment based on chemical and economic properties, Int. J. Hydrogen Energy 44 (2019) 6631–6654. https://doi.org/10.1016/j.ijhydene.2019.01.199

[64] J. Ren, N.M. Musyoka, H.W. Langmi, M. Mathe, S. Liao, Current research trends and perspectives on materials-based hydrogen storage solutions: A critical review, Int. J. Hydrogen Energy 42 (2017) 289–311. https://doi.org/10.1016/j.ijhydene.2016.11.195

[65] U. Eberle, M. Felderhoff, F. Schüth, Chemical and physical solutions for hydrogen storage, Angew. Chemie - Int. Ed. 48 (2009) 6608–6630. https://doi.org/10.1002/anie.200806293

[66] W.F. Pacheco, F.S. Semaan, V.G.K. De Almeida, A.G.S.L. Ritta, R.Q. Aucélio, Voltammetry: A brief review about concepts, Rev. Virtual Quim. 5 (2013) 516–537. https://doi.org/10.5935/1984-6835.20130040

[67] B. Speiser, Linear Sweep and Cyclic Voltammetry, Encycl. Electrochem. (2003). https://doi.org/10.1002/9783527610426.bard030201

[68] T.W. Napporn, Y. Holade, B. Kokoh, S. Mitsushima, K. Mayer, B. Eichberger, V. Hacker, Electrochemical measurement methods and characterization on the cell level, 2018. https://doi.org/10.1016/B978-0-12-811459-9.00009-8

[69] J.E. Baur, Handbook of Electrochemistry, Handb. Electrochem. (2007) 829–848. https://doi.org/10.1016/B978-044451958-0.50036-7

[70] D.S. Hall. (2015) An Electrochemical and Spectroscopic Investigation of Nickel Electrodes in Alkaline Media for Applications in Electro-Catalysis an Electrochemical and Spectroscopic Investigation of Nickel (Doctoral dissertation, Cambridge University). https://www.researchgate.net/publication/272786543_An_Electrochemical_and_Spectroscopic_Investigation_of_Nickel_Electrodes_in_Alkaline_Media_for_Applications_in_Electro-Catalysis

[71] B. Díaz, L. Freire, M.F. Montemor, X.R. Nóvoa, Oxide film growth by CSV on AISI 316L: A combined electrochemical and analytical characterization, J. Braz. Chem. Soc. 24 (2013) 1246–1258. https://doi.org/10.5935/0103-5053.20130158

[72] B. Pierozynski, T. Mikolajczyk, On the Temperature Dependence of Hydrogen Evolution Reaction at Nickel Foam and Pd-Modified Nickel Foam Catalysts, Electrocatalysis 6 (2014) 51–59. https://doi.org/10.1007/s12678-014-0216-z

[73] D.S.P. Cardoso, L. Amaral, D.M.F. Santos, B. Šljukić, C.A.C. Sequeira, D. Macciò, A. Saccone, Enhancement of hydrogen evolution in alkaline water electrolysis by using nickel-rare earth alloys, Int. J. Hydrogen Energy 40 (2015) 4295–4302. https://doi.org/10.1016/j.ijhydene.2015.01.174

[74] E. Cossar, M.S.E. Houache, Z. Zhang, E.A. Baranova, Comparison of electrochemical active surface area methods for various nickel nanostructures, J. Electroanal. Chem. 870 (2020) 114246. https://doi.org/10.1016/j.jelechem.2020.114246

[75] AGFA, Technical Data Sheet ZIRFON PERL UTP 500 (2020). https://www.agfa.com/specialty-products/wp-content/uploads/sites/8/2020/06/TDS_ZIRFON_PERL_UTP_500_20200525.pdf (acessed August, 8)

[76] A.L. Woo, Conductance Studies of Concentrated Solutions of Sodium Hydroxide and Potassium Hydroxide Electrolytes, (1968). Electronic Theses and Dissertation. 3516. http://openprairie.sdstate.edu/etd/3516

# A APPENDIX

## A.1 IONIC RESISTANCE OF THE ZIRFON PERL UTP 500 MEMBRANE

**Table 12 – Ionic resistance of the Zirfon Perl UTP 500 membrane of 30 wt.% KOH solution at different temperatures [75].**

| 30 wt.% KOH | |
|---|---|
| T / ºC | $R_{membrane}$ / Ω.cm$^2$ |
| 30 | 0.28 |
| 60 | 0.18 |
| 90 | 0.10 |

## A.2 SPECIFIC CONDUCTIVITY VALUES

### A.2.1 KOH

**Table 13 - Specific conductivity of 30 wt.% KOH solutions at different temperatures. Adapted from [47].**

| 30 wt. % | |
|---|---|
| T / ºC | $\sigma_{electrolyte}$ / S cm$^{-1}$ |
| 0 | 0.3434 |
| 10 | 0.4474 |
| 20 | 0.5610 |
| 25 | 0.6211 |
| 30 | 0.6831 |
| 40 | 0.8125 |
| 50 | 0.9479 |
| 60 | 1.0885 |
| 70 | 1.2334 |
| 80 | 1.3816 |
| 90 | 1.5327 |
| 100 | 1.6857 |

### A.2.2 NaOH

**Table 14 - Specific conductivity of a 30 wt.% NaOH solution at different temperatures. Adapted from [76].**

| 30 wt.% | |
|---|---|
| T / ºC | $\sigma_{electrolyte}$ / S cm$^{-1}$ |
| 25 | 0.2646 |
| 35 | 0.3592 |
| 45 | 0.4992 |
| 55 | 0.6373 |
| 65 | 0.8008 |
| 80 | 0.9845 |

## A.3 Implementations of the theoretical behavior of the electrolyzer in MATLAB/Simulink

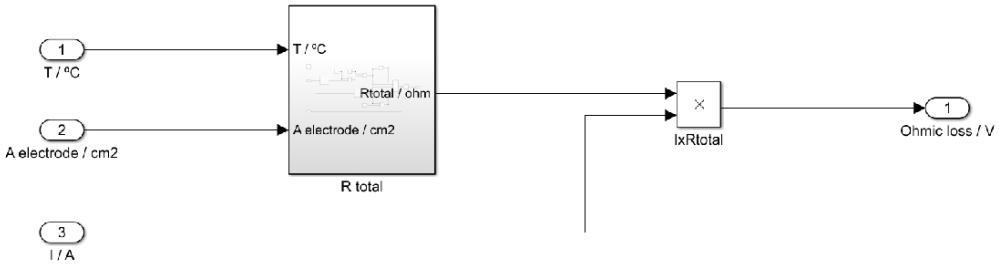


**Figure 35 – Implementation of the ohmic losses.**

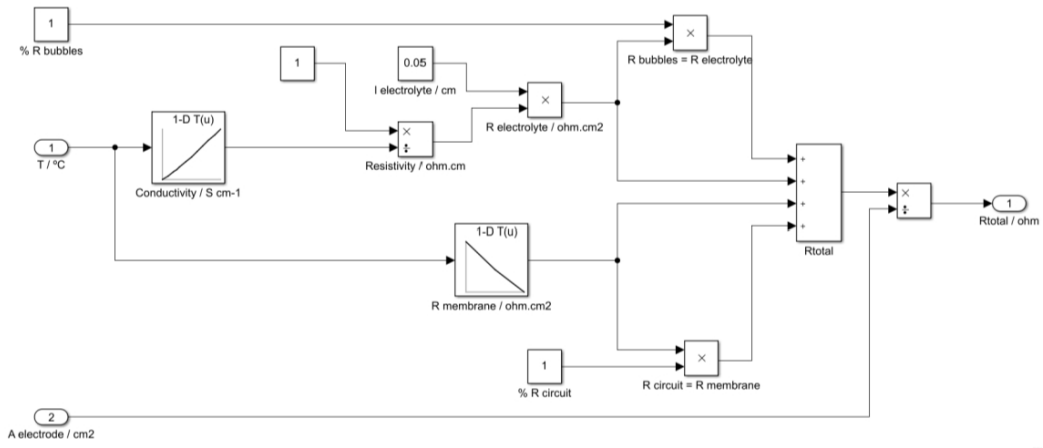


**Figure 36 – Implementation of the resistance of the cell.**

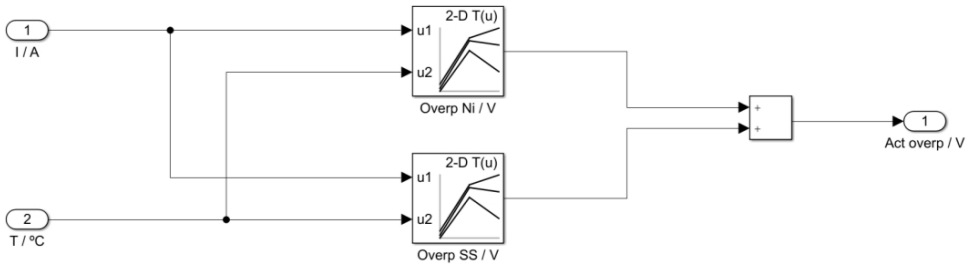


**Figure 37 – Implementation of the activation overpotential.**

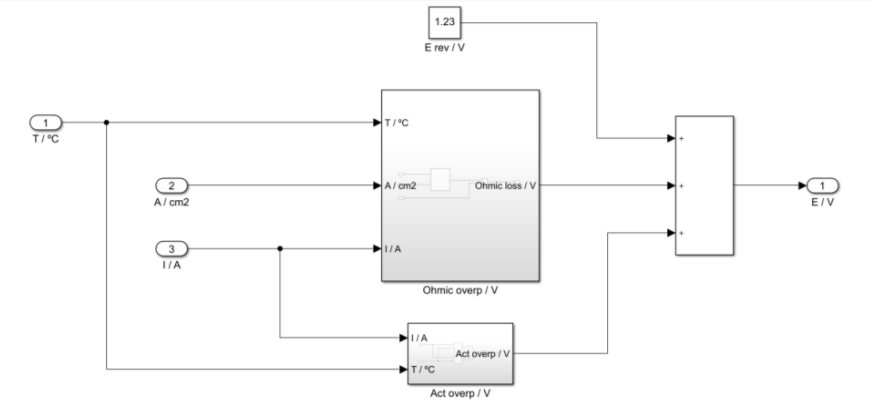


**Figure 38 - Implementation of the cell potential.**

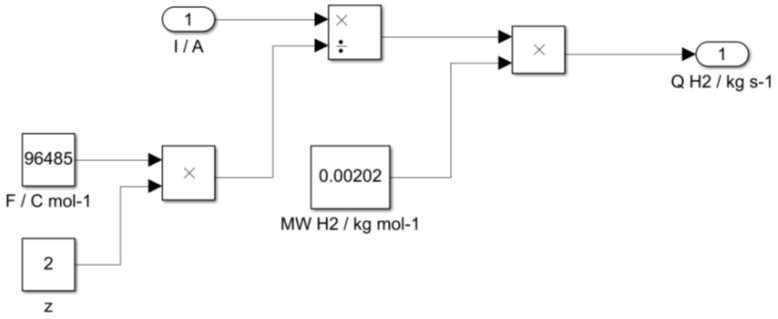


**Figure 39 – Implementation of the theoretical hydrogen production.**

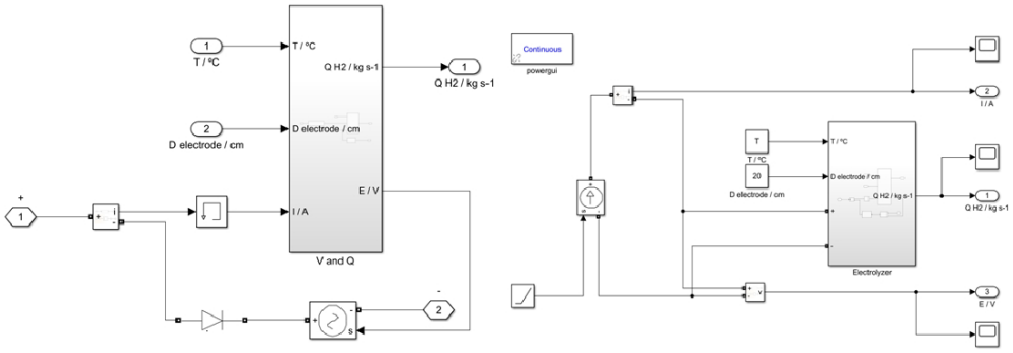


**Figure 40 – (a) Implementation of the electrolyzer system and (b) implementation to obtain the polarization curves of the electrolyzer.**